

A 38 Million Year Old Neptune-Sized Planet in the Kepler Field

² L. G. BOUMA,^{1,2,*} J. L. CURTIS,^{3,4} K. MASUDA,⁵ L. A. HILLENBRAND,¹ G. STEFANSSON,^{2,†} H. ISAACSON,⁶
³ N. NARITA,^{7,8,9,10} A. FUKUI,^{7,10} M. IKOMA,¹¹ M. TAMURA,^{12,9,11} A. L. KRAUS,¹³ E. FURLAN,¹⁴
⁴ C. L. GNILKA,^{15,14} K. V. LESTER,¹⁵ AND S. B. HOWELL¹⁵

⁵ Cahill Center for Astrophysics, California Institute of Technology, Pasadena, CA 91125, USA

⁶ Department of Astrophysical Sciences, Princeton University, 4 Ivy Lane, Princeton, NJ 08540, USA

⁷ Department of Astronomy, Columbia University, 550 West 120th Street, New York, NY 10027, USA

⁸ Department of Astrophysics, American Museum of Natural History, New York, NY 10024, USA

⁹ Department of Earth and Space Science, Osaka University, Osaka 560-0043, Japan

¹⁰ Astronomy Department, University of California, Berkeley, CA 94720, USA

¹¹ Komaba Institute for Science, The University of Tokyo, Tokyo 153-8902, Japan

¹² Japan Science and Technology Agency, PRESTO, Tokyo 153-8902, Japan

¹³ Astrobiology Center, Tokyo 181-8588, Japan

¹⁴ Instituto de Astrofísica de Canarias (IAC), 38205 La Laguna, Tenerife, Spain

¹⁵ Division of Science, National Astronomical Observatory of Japan, Tokyo 181-8588, Japan

¹⁶ Department of Astronomy, The University of Tokyo, Tokyo 113-0033, Japan

¹⁷ Department of Astronomy, The University of Texas at Austin, Austin, TX 78712, USA

¹⁸ NASA Exoplanet Science Institute, Caltech/IPAC, Pasadena, CA 91125, USA

¹⁹ NASA Ames Research Center, Moffett Field, CA 94035, USA

(Received 2021 Oct 12; Revised —; Accepted —)

Submitted to AAS Journals

ABSTRACT

Kepler 1627A is a G8V star previously known to host a $3.8 R_{\oplus}$ (**Replaced:** mini-Neptune replaced with: planet) on a 7.2 day orbit. The star was observed by the Kepler space telescope because it is nearby ($d = 329$ pc) and it resembles the Sun. Here we show using Gaia kinematics, TESS stellar rotation periods, and spectroscopic lithium abundances that Kepler 1627 is a member of the 38^{+6}_{-5} Myr old δ Lyr cluster. To our knowledge, this makes Kepler 1627Ab the youngest planet with a precise age yet found by the (**Replaced:** main replaced with: prime) Kepler mission. The Kepler photometry shows two peculiarities: the average transit profile is asymmetric, and the individual transit times might be correlated with the local light curve slope. We discuss possible explanations for each anomaly. More importantly, the δ Lyr cluster is one of $\sim 10^3$ coeval groups whose properties have been clarified by Gaia. Many other exoplanet hosts are candidate members of these clusters; their ages can be verified (**Replaced:** through replaced with: with) the trifecta of Gaia, TESS, and ground-based spectroscopy.

Keywords: exoplanet evolution (491), open star clusters (1160), stellar ages (1581)

1. INTRODUCTION

While thousands of exoplanets have been discovered orbiting nearby stars, the vast majority of

them are several billion years old. This makes it difficult to test origin theories for the different families of planets, since many evolutionary processes are expected to operate on timescales of less than 100 million years.

For instance, the “mini-Neptunes”, thought to be made of metal cores, silicate mantles (Kite et al. 2020), and extended hydrogen-dominated atmospheres, are expected to shrink in size by fac-

Corresponding author: L. G. Bouma
luke@astro.caltech.edu

* 51 Pegasi b Fellow

† Henry Norris Russell Fellow

tors of several over their first 10^8 years. Specifically, in the models of Owen & Wu (2016) and Owen (2020), the $\approx 5 M_\oplus$ planets start with sizes of $4 - 12 R_\oplus$ shortly after the time of disk dispersal ($\lesssim 10^7$ years), and shrink to sizes of $2 - 4 R_\oplus$ by 10^8 years. While the majority of this change is expected to occur within the first few million years after the disk disperses (Ikoma & Hori 2012), stellar irradiation and internal heat can also power gradual outflows which, if strong enough, can deplete or entirely strip the atmosphere (Lopez et al. 2012; Owen & Wu 2013; Ginzburg et al. 2018). Discovering young planets, measuring their masses, and detecting their atmospheric outflows are key steps toward testing this paradigm, which is often invoked to explain the observed radius distribution of mature exoplanets (Fulton et al. 2017; Van Eylen et al. 2018).

The K2 and TESS missions have now enabled the detection of about ten close-in planets younger than 100 million years, all smaller than Jupiter (Mann et al. 2016; David et al. 2016, 2019; Newton et al. 2019; Bouma et al. 2020; Plavchan et al. 2020; Rizzuto et al. 2020; Martioli et al. 2021). The Kepler mission however has not yielded any planets with precise ages below one gigayear (Meibom et al. 2013). The reason is that during the (Replaced: main replaced with: prime) Kepler mission (2009–2013), only four open clusters were known in the Kepler field, with ages spanning 0.7 Gyr to 9 Gyr (Meibom et al. 2011). Though isochronal, gyrochronal, and lithium-based analyses suggest that younger Kepler planets do exist (Walkowicz & Basri 2013; Berger et al. 2018; David et al. 2021), accurate and precise age measurements typically require an ensemble of stars. Fortunately, recent analyses of the Gaia data have greatly expanded our knowledge of cluster memberships (e.g., Cantat-Gaudin et al. 2018; Zari et al. 2018; Kounkel & Covey 2019; Meingast et al. 2021; Kerr et al. 2021). As part of our Cluster Difference Imaging Photometric Survey (CDIPS, Bouma et al. 2019), we concatenated the available analyses from the literature, which yielded a list of candidate young and age-dated stars (see Appendix A).

Matching our young star list against stars observed by Kepler revealed that Kepler observed a portion of the δ Lyr cluster (Stephenson-1; Theia 73). More specifically, a clustering analysis of the Gaia data by Kounkel & Covey (2019) reported that Kepler 1627 (KIC 6184894; KOI 5245) is a δ Lyr cluster member. Given the previous statistical validation of the close-in (Replaced: mini-Neptune replaced with: Neptune-sized planet) Kepler 1627b (Tenenbaum et al. 2012; Morton et al. 2016; Thompson et al. 2018), we begin

by scrutinizing the properties of the cluster (Section 2). We find that the δ Lyr cluster is 38^{+6}_{-5} Myr old, and in Section 3 show that Kepler 1627 is both a binary and also a member of the cluster. Focusing on the planet (Section 4), we confirm that despite the existence of the previously unreported M2.5V companion, hereafter Kepler 1627B, the planet orbits the G-dwarf primary, Kepler 1627A. We also analyze an asymmetry in the average transit profile, and a possible correlation between the individual transit times and the local light curve slope. We conclude by discussing broader implications for our ability to age-date a larger sample of planets (Section 5).

2. THE CLUSTER

To measure the age of the δ Lyr cluster, we first selected a set of candidate cluster members (Section 2.1), and then analyzed these stars using a combination of the isochronal and gyrochronal techniques (Section 2.2).

2.1. Selecting Cluster Members

Kounkel & Covey (2019) applied an unsupervised clustering algorithm to Gaia DR2 on-sky positions, proper motions, and parallaxes for stars within the nearest kiloparsec. For the δ Lyr cluster (Theia 73), they reported 3,071 candidate members. We matched these stars against the latest Gaia EDR3 observations using the dr2_neighbourhood table from the ESA archive, taking the stars closest in proper motion and epoch-corrected angular distance as the presumed match (Gaia Collaboration et al. 2021a). In Figure 1, (Added: we)have shown galactic positions only for the stars with parallax signal-to-noise exceeding 20. (Added: We calculated the tangential velocities for each of these stars relative to Kepler 1627 ($\Delta\mu^*$) by subtracting the observed proper motion from what the proper motion at the star’s position would be if it were co-moving with Kepler 1627.)The reported cluster members (gray and black points) extend over a much larger volume (Added: in both physical and kinematic space)than the cluster previously identified by Stephenson (1959) and later corroborated by Eggen (1968). While the non-uniform “clumps” of stars might comprise a *bona fide* cluster of identically-aged stars, they could also be heavily contaminated by field stars. (Added: One reason to suspect this is that the spread in tangential velocities exceeds typical limits for kinematic coherence (Meingast et al. 2021)). We therefore considered stars only in the immediate kinematic and spatial vicinity of Kepler 1627 as candidate cluster members. We performed (Replaced: the replaced with: this) selection cut(Deleted: s) manually, by drawing lassos with

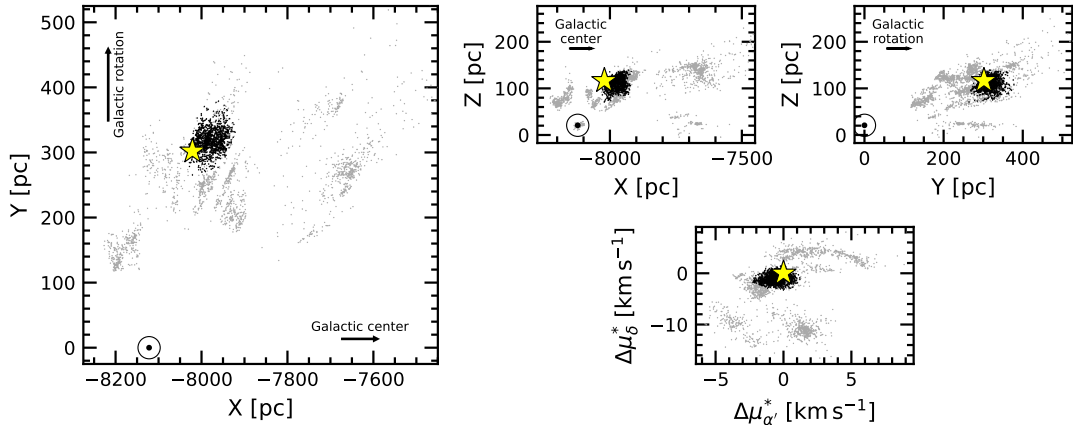


Figure 1. Galactic positions and tangential velocities of stars in the δ Lyr cluster. Points are reported cluster members from Kounkel & Covey (2019). The tangential velocities relative to Kepler 1627 (bottom right) are computed assuming that every star has the same three-dimensional spatial velocity as Kepler 1627. Our analysis considers stars (black points) in the spatial and kinematic vicinity of Kepler 1627 (yellow star). The question of whether the other candidate cluster members (gray points) are part of the cluster is outside our scope. The location of the Sun is (\odot) is shown (Added: to clarify the direction along which parallax uncertainties are expected to produce erroneous clusters).

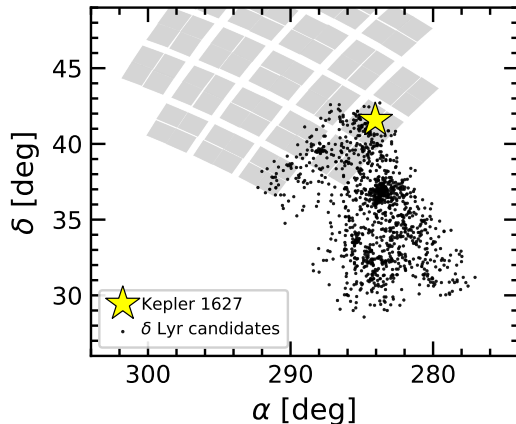


Figure 2. Kepler's view of the δ Lyr cluster, shown in equatorial coordinates. Each black circle is a candidate cluster member selected based on its position and kinematics (Figure 1). Of the 1,201 candidate cluster members, 58 have at least one quarter of Kepler data. TESS has also observed most of the cluster, for one to two lunar months to date.

the interactive `glue` visualization tool (Beaumont et al. 2014) in the four projections shown in Figure 1. The overlap between the Kepler field and the resulting candidate cluster members is shown in Figure 2. While this method will include some field interlopers in the “cluster star” sample, and vice-versa, it should suffice for our aim of verifying the existence of the cluster in the vicinity of Kepler 1627.

2.2. The Cluster’s Age

2.2.1. Color-Absolute Magnitude Diagram

We measured the isochrone age using an empirical approach. The left panel of Figure 3 shows the color-absolute magnitude diagram (CAMD) of candidate δ Lyr cluster members, IC 2602, the Pleiades, and the field. The stars from the Pleiades and IC 2602 were adopted from Cantat-Gaudin et al. (2018), and the field stars are from the Gaia EDR3 Catalog of Nearby Stars (Gaia Collaboration et al. 2021b). We cleaned these following the data filtering criteria from Gaia Collaboration et al. (2018a, Appendix B), except that we weakened the parallax precision requirement to $\varpi/\sigma_\varpi > 5$. (Added: This also involved cuts on the photometric signal to noise ratio, the number of visibility periods used, the astrometric χ^2 of the single-source solution, and the $G_{\text{BP}} - G_{\text{RP}}$ color excess factor.) These filters were designed to include genuine binaries while omitting instrumental artifacts. We then corrected for extinction by querying the 3-dimensional maps of Capitanio et al. (2017) and Lallement et al. (2018)¹, and applied the extinction coefficients $k_X \equiv A_X/A_0$ computed by Gaia Collaboration et al. (2018a) assuming that $A_0 = 3.1E(B-V)$. For IC 2602, the Pleiades, and the δ Lyr cluster, this procedure yielded a respective mean and standard deviation for the reddening of $E(B-V) = \{0.020 \pm 0.003, 0.045 \pm 0.008, 0.032 \pm 0.006\}$. These values (Replaced: agree reasonably well with replaced with: are within a factor of two of) previously reported values (Replaced: from replaced with: in) the literature (e.g., Gaia Collaboration et al. 2018a; Kounkel & Covey 2019; Bossini et al.

¹ <https://stilism.obspm.fr/>, 2021/09/25

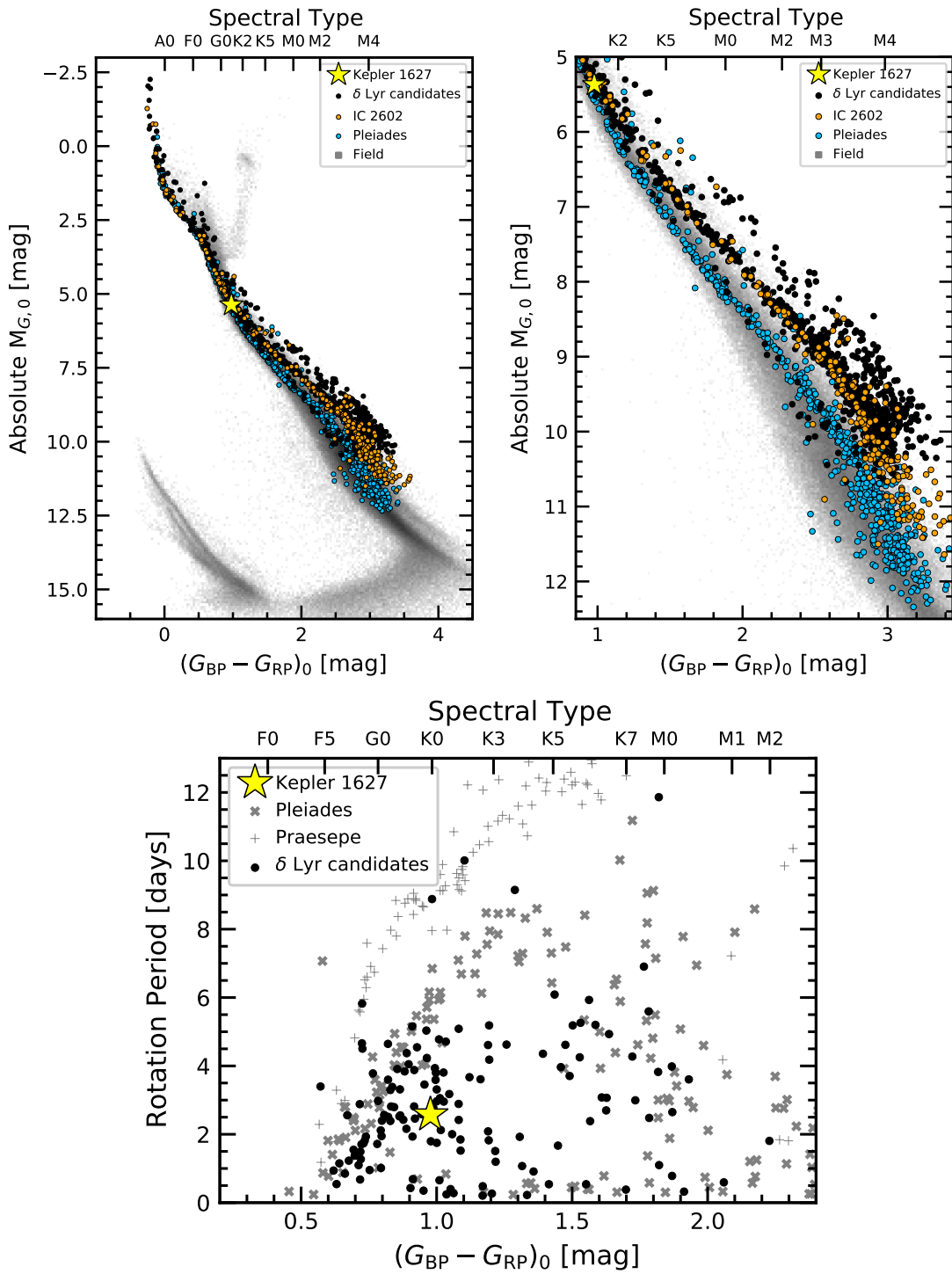


Figure 3. The δ Lyr cluster is 38^{+6}_{-5} Myr old. *Top:* Color-absolute magnitude diagram of candidate δ Lyr cluster members, in addition to stars in IC 2602 (≈ 38 Myr), the Pleiades (≈ 115 Myr), and the Gaia EDR3 Catalog of Nearby Stars (gray background). The zoomed right panel highlights the pre-main-sequence. The δ Lyr cluster and IC 2602 are approximately the same isochronal age. *Bottom:* TESS and Kepler stellar rotation period versus dereddened Gaia color, with the Pleiades and Praesepe (650 Myr) shown for reference (Rebull et al. 2016; Douglas et al. 2017). Most candidate δ Lyr cluster members are gyrochronologically younger than the Pleiades; outliers are probably field interlopers.

204 2019)(Added: , and are all small enough that
 205 the choice of whether to use them vs. other ex-
 206 tinction estimates does not affect our primary
 207 conclusions).

208 Figure 3 shows that the δ Lyr cluster and IC 2602
 209 overlap, and therefore are approximately the same
 210 age. In our exploration, we also compared against
 211 μ -Tau (62 ± 7 Myr; Gagné et al. 2020) and the
 212 Upper-Centaurus-Lupus (UCL) component of the
 213 Sco OB2 association (≈ 16 Myr; Pecaut & Mama-
 214 jek 2016). The pre-main-sequence M dwarfs of the
 215 δ Lyr cluster were intermediate between the lat-
 216 ter two clusters. To turn this heuristic interpola-
 217 tion into an age measurement, we used the empirical
 218 method developed by Gagné et al. (2020). In
 219 brief, we fitted the pre-main-sequence loci of a set
 220 of reference clusters, and the locus of the target δ
 221 Lyr cluster was then modeled as a piecewise linear
 222 combination of these reference clusters. For our
 223 reference clusters, we adopted members of UCL,
 224 IC 2602, and the Pleiades from Damiani et al.
 225 (2019) and Cantat-Gaudin et al. (2018) respec-
 226 tively. We removed binaries by requiring RUWE <
 227 1.3, radial_velocity_error below the 80th
 228 percentile of each cluster’s distribution, and ex-
 229 cluded stars that were obvious photometric bina-
 230 ries in the CAMD.² We then passed a moving box
 231 average and standard deviation across the CAMD
 232 in 0.10 mag bins, fitted a univariate spline to the
 233 binned values, and assembled a piecewise grid
 234 of (Deleted: hybrid–) isochrones spanning the
 235 ages between UCL (Replaced: to replaced with:
 236 and) the Pleiades using Equation(Replaced: s 6
 237 and 7 replaced with: 6) from Gagné et al. (2020).
 238 (Added: To derive a probability distribution
 239 function for the age of δ Lyr cluster, we then
 240 assumed a Gaussian likelihood that treated the
 241 interpolated isochrones as the “model” and the
 242 δ Lyr cluster’s isochrone as the “data” (Equation
 243 7 from Gagné et al. 2020). The cluster’s age
 244 and its statistical uncertainty are then quoted as
 245 the the mean and standard deviation of this age
 246 posterior.)

247 The ages returned by this procedure depend on
 248 the ages assumed for each reference cluster. We
 249 adopted a 115 Myr age for the Pleiades (Dahm
 250 2015), and a 16 Myr age for UCL (Pecaut & Ma-
 251 majek 2016). The age of IC 2602 however is the
 252 most important ingredient, since it receives the
 253 most weight in the interpolation. Plausible ages
 254 for IC 2602 span 30 Myr to 46 Myr, with older ages
 255 being preferred by the lithium-depletion-boundary
 256 (LDB) measurements (Dobbie et al. 2010; Randich

² For a description of the renormalized unit weight error (RUWE), see the GAIA DPAC technical note http://www.rssd.esa.int/doc_fetch.php?id=3757412.

257 et al. 2018) and younger ages by the main-
 258 sequence turn-off (Stauffer et al. 1997; David &
 259 Hillenbrand 2015; Bossini et al. 2019). If we were
 260 to adopt the 30 Myr age for IC 2602, then the δ
 261 Lyr cluster would be 31^{+5}_{-4} Myr old. For the con-
 262 verse extreme of 46 Myr, the δ Lyr cluster would
 263 be 44^{+8}_{-7} Myr old. We adopt an intermediate 38 Myr
 264 age for IC 2602, which yields an age for the δ Lyr
 265 cluster of 38^{+6}_{-5} Myr.³ Follow-up studies of the LDB
 266 or main-sequence turn-off in the δ Lyr cluster could
 267 help determine a more precise and accurate age for
 268 the cluster, and are left for future work.

269 2.2.2. Stellar Rotation Periods

270 Of the 3,071 candidate δ Lyr cluster members re-
 271 ported by Kounkel & Covey (2019), 924 stars were
 272 amenable to rotation period measurements ($G < 17$
 273 and $(G_{\text{BP}} - G_{\text{RP}})_0 > 0.5$) using the TESS full frame
 274 image data. (Added: As a matter of scope, we re-
 275 stricted our attention to the 391 stars discussed
 276 in Section 2.1 in the spatial and kinematic prox-
 277 imity of Kepler 1627.) We extracted light curves
 278 from the TESS images using the nearest pixel to
 279 each star, and regressed them against systematics
 280 with the causal pixel model implemented in the
 281 unpopular package (Hattori et al. 2021). We
 282 then measured candidate rotation periods using a
 283 Lomb-Scargle periodogram (Lomb 1976; Scargle
 284 1982; Astropy Collaboration et al. 2018). To en-
 285 able cuts on crowding, we queried the Gaia source
 286 catalog for stars within a $21.^{\circ}0$ radius of the tar-
 287 get star (a radius of 1 TESS pixel). Within this ra-
 288 dius, we recorded the number of stars with greater
 289 brightness than the target star, and with brightness
 290 within 1.25 TESS magnitudes of the target star.

291 We then cleaned the candidate TESS rotation pe-
 292 riod measurements through a combination of auto-
 293 mated and manual steps. (Deleted: As a matter
 294 of scope, we restricted our attention to the 391
 295 stars discussed in Section 2.1 in the spatial and
 296 kinematic proximity of Kepler 1627.) Kepler
 297 rotation periods were derived by McQuillan et al.
 298 (2014) for 28 of (Replaced: these replaced with:
 299 our 391)stars; for these cases, we simply adopted
 300 the Kepler rotation period. For the remaining stars
 301 with only TESS data, we focused only on the
 302 stars for which no companions were known with
 303 a brightness exceeding one-tenth of the target star
 304 in a $21.^{\circ}0$ radius. There were 192 stars that met
 305 these crowding requirements, and that had TESS
 306 data available. For plotting purposes we then im-

³ Our exploration of the PARSEC and MIST isochrone mod-
 els over a grid of ages, metallicities, and reddenings, yielded
 the best agreement for this ≈ 38 Myr age as well, given
 $[Fe/H] = +0.1$ and $A_V = 0.2$ (Bressan et al. 2012; Choi et al.
 2016); this preferred CAMD reddening is higher than the
 Lallement et al. (2018) value by a factor of two.

posed a selection based on the strength of the signal itself: we required the Lomb Scargle power to exceed 0.2, and the period to be below 15 days.

The lower panel of Figure 3 shows the resulting 145 stars. The majority of these stars fall below the “slow sequence” of the Pleiades, consistent with a gyrochronal age for the δ Lyr cluster below 100 Myr. In fact, the rotation-color distributions of other 30 Myr to 50 Myr clusters (*e.g.*, IC 2602 and IC 2391) are indistinguishable(Added: from each other) (Douglas et al. 2021). Approximately 10 of the δ Lyr cluster stars appear as outliers above the “slow sequence”. Assuming that they are all false positives (*i.e.*, field interlopers), our rotation period detection fraction would be $135/192 \approx 70\%$. (Replaced: The other stars are likely to be field contaminants. replaced with: Although some of these outlier stars might be unresolved F+K binaries that are in the cluster (Stauffer et al. 2016), assuming that they are field contaminants provides a more secure lower bound of the rotation period detection fraction.) A final possible confounding factor – binarity – is known to affect the “fast sequence” of stars beneath the slow sequence (Meibom et al. 2007; Gillen et al. 2020; Bouma et al. 2021). We do not expect it to change the central conclusion regarding the cluster’s age.

3. THE STARS

3.1. Kepler 1627A

3.1.1. Age

Based on the spatial and kinematic association of Kepler 1627 with the δ Lyr cluster, and the assumption that the planet formed shortly after the star, it seems likely that Kepler 1627 is the same age as the cluster. There are two consistency checks on whether this is true: rotation and lithium. Based on the Kepler light curve, the rotation period is 2.642 ± 0.042 days, where the quoted uncertainty is based on the scatter in rotation periods measured from each individual Kepler quarter. This is consistent with comparable cluster members (Figure 3).

To infer the amount of Li I from the 6708 Å doublet (*e.g.*, Soderblom et al. 2014), we acquired an iodine-free spectrum from Keck/HIRES on the night of 2021 March 26 using the standard setup and reduction techniques of the California Planet Survey (Howard et al. 2010). Following the equivalent width measurement procedure described by Bouma et al. (2021), we find $\text{EW}_{\text{Li}} = 233^{+5}_{-7}$ mÅ. This value does not correct for the Fe I blend at 6707.44 Å. Nonetheless, given the stellar effective temperature (Table 1), this measurement is in agreement with expectations for a ≈ 40 Myr star (*e.g.*, as measured in IC 2602 by Randich et al. 2018). It is also larger than any lithium equivalent

widths measured by Berger et al. (2018) in their analysis of 1,301 Kepler-star spectra.

3.1.2. Stellar Properties

The adopted stellar parameters are listed in Table 1. The stellar mass, radius, and effective temperature are found by interpolating against a 38 Myr MIST isochrone (Choi et al. 2016). The statistical uncertainties are propagated from the absolute magnitude (mostly originating from the parallax uncertainty) and the color; the systematic uncertainties are taken to be the difference between the PARSEC (Bressan et al. 2012) and MIST isochrones. Reported uncertainties are a quadrature sum of the statistical and systematic components. As a consistency check, we analyzed the aforementioned Keck/HIRES spectrum from the night of 2021 March 26 using a combination of SpecMatch-Emp for stellar properties, and SpecMatch-Synth for $v\sin i$ (Yee et al. 2017). This procedure yielded $T_{\text{eff}} = 5498 \pm 100$ K, $\log g = 4.6 \pm 0.1$, $[\text{Fe}/\text{H}] = 0.15 \pm 0.10$ from SpecMatch-Emp, and $v\sin i = 18.9 \pm 1.0$ from SpecMatch-Synth. These values are within the $1-\sigma$ uncertainties of our adopted values from the isochrone interpolation.

3.2. Kepler 1627B

We first noted the presence of a close neighbor in the Kepler 1627 system on 2015 July 22 when we acquired adaptive optics imaging using the NIRC2 imager on Keck-II. We used the narrow camera (FOV = 10.2'') to obtain 8 images in the K' filter ($\lambda = 2.12 \mu\text{m}$) with a total exposure time of 160 s. We analyzed these data following Kraus et al. (2016), which entailed using PSF-fitting to measure the separation, position angle, and contrast of the candidate companion. The best-fitting empirical PSF template was identified from among the near-contemporaneous observations of single stars in the same filter. The mean values inferred from the 8 images are reported in Table 1. To estimate the detection limits, we analyzed the residuals after subtracting the empirical PSF template. Within each residual image, the flux was measured through 40 mas apertures centered on every pixel, and then the noise as a function of radius was estimated from the RMS within concentric rings. Finally, the detection limits were estimated from the strehl-weighted sum of the detection significances in the image stack, and we adopted the $6-\sigma$ threshold as the detection limit for ruling out additional companions.

We also observed Kepler 1627 on Gemini-North using the ‘Alopeke speckle imager on 2021 June 24. ‘Alopeke is a dual-channel speckle interferometer that uses narrow-band filters centered at

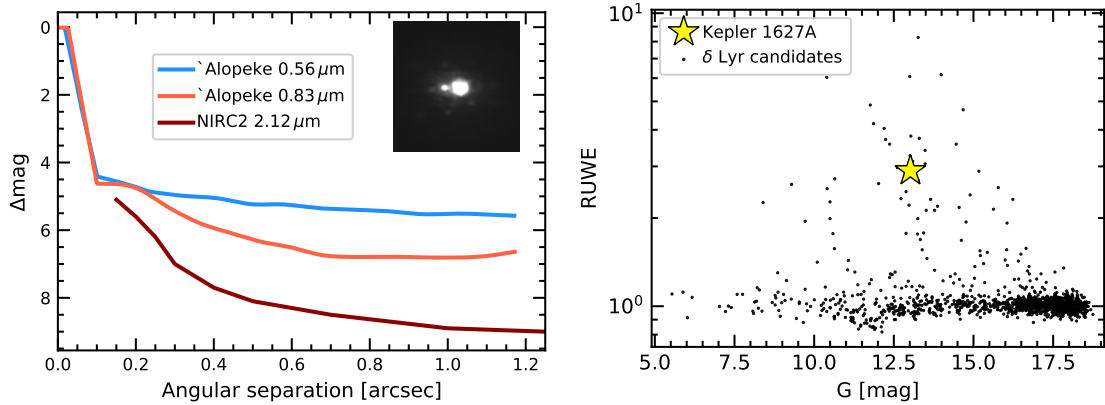


Figure 4. Kepler 1627 is a binary. *Left:* High-resolution imaging from Gemini-North/‘Alopeke and Keck/NIRC2 shows an \approx M2.5V companion at $\rho \approx 0.^{\prime\prime}16$, which corresponds to a projected separation of 53 ± 4 AU. The inset shows a cutout of the stacked NIRC2 image (North is up, East is left, scale is set by the separation of the binary). The lines show $5-\sigma$ contrast limits for the ‘Alopeke filters, and $6-\sigma$ contrast limits for NIRC2 outside of $0.^{\prime\prime}15$. *Right:* Gaia EDR3 renormalized unit weight error (RUWE) point estimates for candidate δ Lyr cluster members. Since other members of the cluster with similar brightnesses have comparable degrees of photometric variability, the high RUWE independently suggests that Kepler 1627 is a binary.

417 0.83 μ m and 0.56 μ m. We acquired three sets
 418 of 1000×60 msec exposures during good seeing
 419 ($0.45''$), and used the autocorrelation function of
 420 these images to reconstruct a single image and 5-
 421 σ detection limits (see Howell et al. 2011). This
 422 procedure yielded a detection of the companion in
 423 the 0.83 μ m notch filter, but not the 0.56 μ m filter.
 424 The measured projected separation and magnitude
 425 difference are given in Table 1.

426 Figure 4 summarizes the results of the high-
 427 resolution imaging. The Gaia EDR3 parallax for
 428 the primary implies a projected separation of $53 \pm$
 429 4 AU, assuming the companion is bound. Al-
 430 though the companion is unresolved in the Gaia
 431 source catalog (there are no comoving, codistant
 432 candidate companions brighter than $G < 20.5$ mag
 433 within $\rho < 120''$), its existence was also suggested
 434 by the primary star’s large (**Replaced: renor-
 435 malized unit weight error (RUWE)**, replaced with:
 436 **RUWE**) relative to other members of the δ Lyr
 437 cluster (**Added: (RUWE \approx 2.9; roughly the 98th
 438 percentile of the cluster’s distribution)**). Based
 439 on the apparent separation, the binary orbital per-
 440 iod is of order hundreds of years. The large
 441 RUWE is therefore more likely to be caused by a
 442 PSF-mismatch skewing the Gaia centroiding dur-
 443 ing successive scans, rather than true astrometric
 444 motion. Regardless, given the low geometric prob-
 445 ability that a companion imaged at $\rho \approx 0.^{\prime\prime}16$ is a
 446 chance line-of-sight companion, we proceed under
 447 the assumption that the companion is bound, and
 448 that Kepler 1627 is a binary. Given the distance
 449 and age, the models of Baraffe et al. (2015) im-
 450 plify a companion mass of $M_B \approx 0.33M_{\odot}$ and com-
 451 panion temperature of $T_{\text{eff},B} \approx 3450$ K. The corre-

452 sponding spectral type is roughly M2.5V (Pecaut
 453 & Mamajek 2013). These models combined with
 454 the NIRC2 contrast limits imply physical limits on
 455 tertiary companions of $M_{\text{ter}} < 50M_{\text{Jup}}$ at $\rho = 50$ AU,
 456 $M_{\text{ter}} < 20M_{\text{Jup}}$ at $\rho = 100$ AU, and $M_{\text{ter}} < 10M_{\text{Jup}}$ at
 457 $\rho = 330$ AU.

4. THE PLANET

4.1. Kepler Light Curve

460 The Kepler space telescope observed Kepler 1627
 461 at a 30-minute cadence from 2009 May 2 until
 462 2013 April 8. Data gaps during quarters 4, 9, and
 463 13 led to an average duty cycle over the 3.9 year
 464 interval of 67%. Kepler 1627 was also observed at
 465 1-minute cadence from 2012 Oct 5 until 2013 Jan
 466 11. The top panel of Figure 5 shows a portion of the
 467 30-minute cadence PDCSAP light curve. Nonas-
 468 trophysical variability has been removed using the
 469 methods discussed by Smith et al. (2017); the de-
 470 fault optimal aperture was assumed (Smith et al.
 471 2016). Cadences with non-zero quality flags (9%
 472 of the data) have been omitted. The resulting pho-
 473 tometry is dominated by a quasi-periodic starspot
 474 signal with a peak-to-peak amplitude that varies
 475 between 2% and 8%. (**Added: Given that the**
 476 **secondary companion’s brightness in the Kepler**
 477 **band is \approx 1.5% that of the primary, source con-**
 478 **fusion for the rotation signal is not expected to**
 479 **be an issue.**) Previous analyses have identified
 480 and characterized the smaller transit signal (Tenen-
 481 baum et al. 2012; Thompson et al. 2018), validated
 482 its planetary nature (Morton et al. 2016), and even
 483 searched the system for transit timing variations
 484 (Holczer et al. 2016). Nonetheless, since the clus-
 485 ter membership provides us with more precise stel-

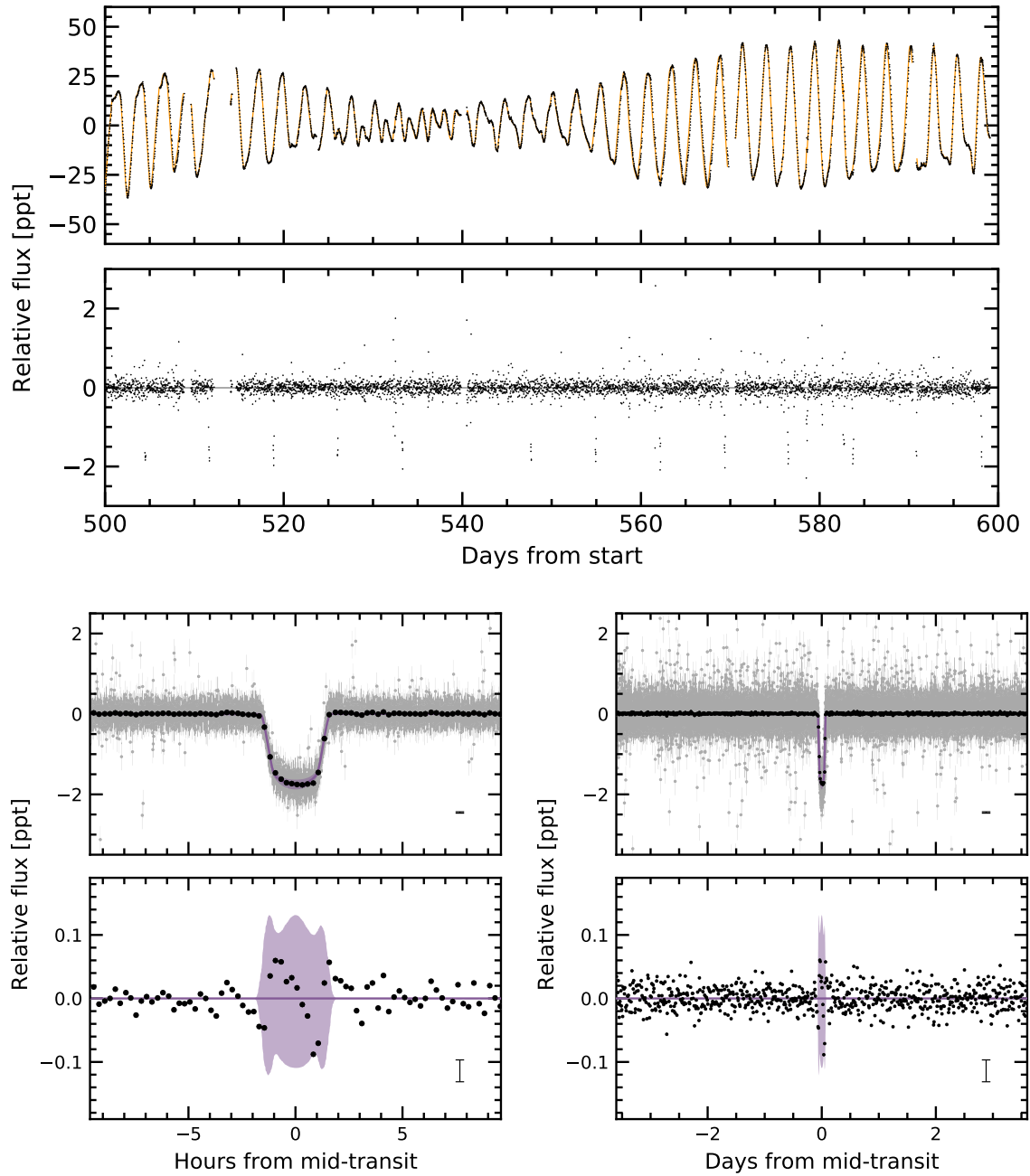


Figure 5. The light curve of Kepler 1627. *Top:* The Kepler data span 1,437 days (3.9 years), sampled at 30 minute cadence; a 100 day segment is shown. The top panel shows the PDCSAP median-subtracted flux in units of parts-per-thousand ($\times 10^{-3}$). The dominant signal is induced by starspots. The stellar variability model (orange line) is subtracted below, revealing the transits of Kepler 1627Ab. The online Figure Set spans the entire 3.9 years of observations. *Bottom:* Phase-folded transit of Kepler 1627Ab with stellar variability removed. Windows over 20 hours (*left*) and the entire orbit (*right*) are shown, and the residual after subtracting the transit is in the bottom-most row. The 2- σ model uncertainties and the best-fit model are the light purple band and the dark purple line. Gray points are individual flux measurements; black points bin these to 15 minute intervals, and have a representative 1- σ error bar in the lower right of each panel. The asymmetric residual during transit is larger than the out-of-transit scatter.

486 lar parameters than those previously available, we
 487 opted to reanalyze the light curve.

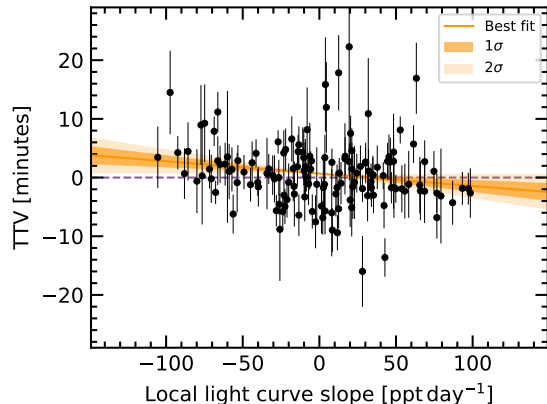
488 4.1.1. Transit and Stellar Variability Model

489 We fitted the Kepler long cadence time series
 490 with a model that simultaneously included
 491 the planetary transit and the stellar variability.
 492 The stellar variability was modeled with
 493 the RotationTerm Gaussian Process kernel in
 494 exoplanet (Foreman-Mackey et al. 2020). This
 495 kernel assumes that the variability is generated by
 496 a mixture of two damped simple harmonic oscil-
 497 lators with characteristic frequencies set by $1/P_{\text{rot}}$
 498 and its first harmonic. We additionally included a
 499 jitter term to inflate the flux uncertainties in a man-
 500 ner that accounted for otherwise unmodeled excess
 501 white noise, and let the eccentricity float. For the
 502 limb-darkening, we assumed a quadratic law, and
 503 sampled using the uninformative prior suggested
 504 by Kipping (2013).

505 Our model therefore included 10 free parameters
 506 for the transit ($\{P, t_0, \delta, b, u_1, u_2, R_*, \log g, e, \omega\}$), 2
 507 free parameters for the light curve normalization
 508 and a white noise jitter ($\{\langle f \rangle, \sigma_f\}$), and 5 hyper-
 509 parameters for the GP ($\{\sigma_{\text{rot}}, P_{\text{rot}}, Q_0, dQ, f\}$). We
 510 also considered including an additive SHOTerm
 511 kernel to account for stochastic noise, but found
 512 that this did not affect the results, and so opted for
 513 the simpler GP kernel. We fitted the models using
 514 PyMC3 (Salvatier et al. 2016; Theano Devel-
 515 opment Team 2016), and accounted for the finite
 516 integration time of each exposure in the numerical
 517 integration when evaluating the model light curve
 518 (see Kipping 2010). We assumed a Gaussian like-
 519 lihood, and after initializing each model with the
 520 parameters of the maximum *a posteriori* model,
 521 we sampled using PyMC3’s gradient-based No-U-
 522 Turn Sampler (Hoffman & Gelman 2014) in the
 523 bases indicated in Table 2. We used \hat{R} as our con-
 524 vergence diagnostic (Gelman & Rubin 1992).

525 Figure 5 shows the resulting best-fit model in
 526 orange (top) and purple (bottom). The model
 527 parameters and their uncertainties, given in Ta-
 528 ble 2, are broadly consistent with a (Replaced:
 529 mini-Neptune replaced with: Neptune-) sized
 530 planet ($3.82 \pm 0.16 R_{\oplus}$) on a close-in circular⁴
 531 orbit around a G8V host star ($0.88 \pm 0.02 R_{\odot}$). This
 532 best-fit planet size is consistent with those previ-
 533 ously reported by Morton et al. (2016) and Berger
 534 et al. (2018), and corrects for the small amount of
 535 flux dilution from Kepler 1627B.

536 4.1.2. Transit Asymmetry



537 **Figure 6. Possible evidence for a prograde orbit of**
Kepler 1627 Ab. The time of each Kepler transit was
 538 measured, along with the local slope of the light curve.
 539 The two quantities are weakly anti-correlated ($\approx 2-\sigma$),
 540 which might be caused by starspot crossings during the
 541 first (second) half of transit inducing a positive (negative)
 542 TTV, provided that the orbit is prograde (Mazeh et al.
 543 2015). The units along the abscissa can be understood
 544 by considering that the stellar flux changes by ~ 60 ppt
 545 per half rotation period (~ 1.3 days).

546 The transit fit however is not perfect: the lower
 547 panels of Figure 5 show an asymmetric residual in
 548 the data relative to the model: the measured flux
 549 is high during the first half of transit, and low in
 550 the second half. The semi-amplitude of this devi-
 551 ation is ≈ 50 ppm, which represents a $\approx 3\%$ dis-
 552 tortion of the transit depth ($\delta = 1759 \pm 62$ ppm).
 553 Note that although this asymmetry is within the 2-
 554 σ model uncertainties, the model has a jitter term
 555 that grows to account for excess white noise in the
 556 flux. The significance of the asymmetry is there-
 557 fore best assessed in comparison against the intrin-
 558 sic out-of-transit scatter in the data (≈ 16 ppm), not
 559 the model uncertainties. The lower right panel of
 560 Figure 5 demonstrates that the scatter during transit
 561 is higher than during all other phases of the planet’s
 562 orbit.

563 To determine whether the asymmetry could be a
 564 systematic caused by our stellar variability model,
 565 we explored an alternative approach in which we
 566 isolated each transit window, locally fitted out
 567 polynomial trends, and then binned all the ob-
 568 served transits; the asymmetry was still present at
 569 a comparable amplitude. Appendix B describes a
 570 more detailed analysis, which finds that the asym-
 571 metry also seems to be robust to different meth-
 572 ods of data binning in time and by local light curve
 573 slope. Possible astrophysical explanations are dis-
 574 cussed in Section 5.

566 ⁴ Our transit fitting yields $e < 0.48$ at $2-\sigma$; the constraints on the
 eccentricity are not particularly strong.

566 4.1.3. Transit Timing and the Local Slope

The previous analysis by Holczer et al. (2016) did not find any significant long-term transit timing or duration variations (TTVs or TDVs) for Kepler 1627. Quantitatively, the mean and standard deviation of the TTVs and TDVs they measured were -1.1 ± 13.8 min and -3.3 ± 22.1 min. In an earlier analysis however, Holczer et al. (2015) studied correlations between TTVs and local light curve slopes, and for Kepler 1627 found a weak correlation of -29 ± 13 min day $^{-1}$ between the two quantities. Given the possible connection between such correlations and the unresolved starspot crossings that we expect to be present in the Kepler 1627 light curve (Mazeh et al. 2015), we opted to re-examine the individual transit times.

We therefore isolated each of the 144 observed transits to within ± 4.5 hr of each transit, and fitted each window with both *i*) a local polynomial baseline plus the transit, and *ii*) a local linear trend. We considered the results both for a second and fourth-order time-dependence in the local baseline. We let the mid-time of each transit float, and then calculated the residual between the measured mid-time and that of a periodic orbit. This residual, the transit timing variation, is plotted in Figure 6 against the local linear slope for the fourth-order polynomial baseline. The slope of -21 ± 10 min day $^{-1}$ is similar to that found by Holczer et al. (2015).

One concern we had in this analysis was whether our transit fitting procedure might induce spurious correlations between the slope and transit time. In particular, using the second-order polynomial baseline yielded a larger anti-correlation between the TTVs and local slopes, of -79 ± 14 min day $^{-1}$. We therefore performed an injection-recovery procedure in which we injected transits at different phases in the Kepler 1627 light curve and repeated the TTV analysis. This was done at ≈ 50 phases, each separated by $0.02 P_{\text{orb}}$ while omitting the phases in transit. For the second-order polynomial baseline, this procedure yielded a similar anti-correlation in the injected transits as that present in the real transit; using this baseline would therefore bias the result. However for the fourth-order baseline, the correlation present in the data was stronger than in all but one of the injected transits. Possible interpretations are discussed below. Given the statistical significance, this analysis should be interpreted as suggestive at best.

4.2. Planet Confirmation

If the Kepler 1627Ab transit signal is created by a genuine planet, then to our knowledge it would be the youngest planet yet found by the (Replaced:

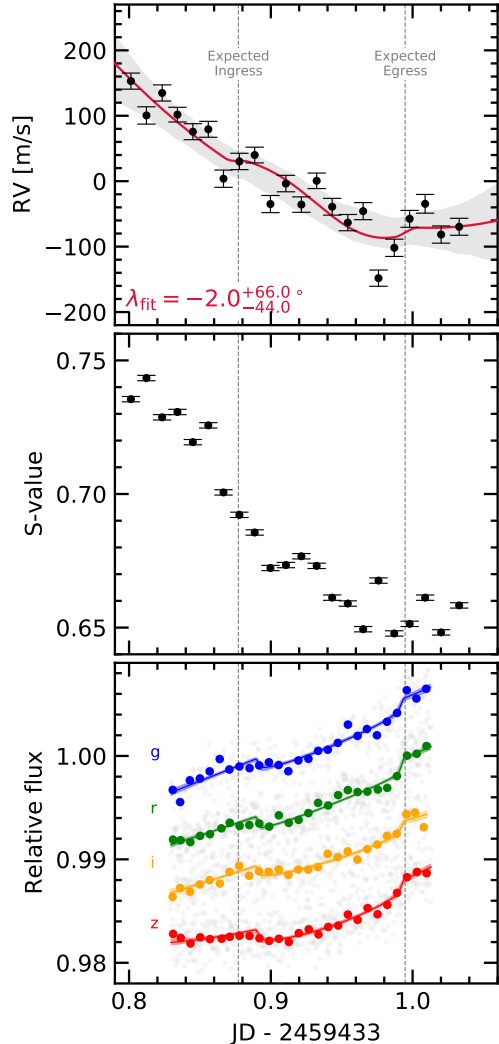


Figure 7. Keck/HIRES radial velocities and MuSCAT3 photometry from the transit of 2021 Aug 7. *Top:* The radial velocity jitter across the 15 minute exposures ($\sigma_{\text{RV}} \approx 30 \text{ m s}^{-1}$) prevented us from detecting the RM effect; a model including the RM anomaly and a quadratic trend in time to fit the spot-induced $\approx 250 \text{ m s}^{-1}$ trend is shown (see Appendix C). Shaded bands show $2-\sigma$ model uncertainties. *Middle:* The RV variations are strongly correlated with varying emission in the Ca H and K lines. *Bottom:* The photometric transit depths are consistent across the *griz* bandpasses. The photometry is binned at 10 minute intervals.

main replaced with: prime) Kepler mission.⁵ Could the transit be produced by anything other than a planet orbiting this near-solar analog? Mor-

⁵ The re-purposed K2 mission however has found two younger systems containing five planets: K2-33b (9 ± 1 Myr; Mann et al. 2016; David et al. 2016) and V1298 Tau (23 ± 4 Myr; David et al. 2019).

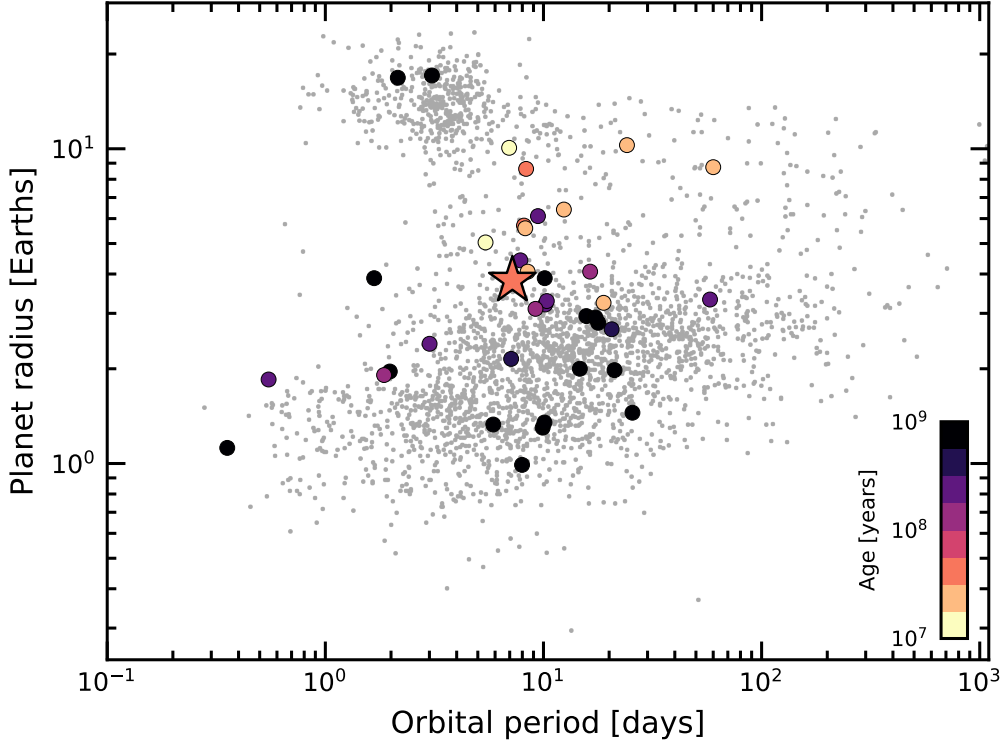


Figure 8. Radii, orbital periods, and ages of transiting exoplanets. Planets younger than a gigayear with $\tau/\sigma_\tau > 3$ are emphasized, where τ is the age and σ_τ is its uncertainty. Kepler 1627Ab is shown with a star. The large sizes of the youngest transiting planets could be explained by their primordial atmospheres not yet having evaporated; direct measurements of the atmospheric outflows or planetary masses would help to confirm this expectation. Selection effects may also be important. Parameters are from the NASA Exoplanet Archive (2021 Sept 15).

ton et al. (2016) validated the planet based on the transit shape, arguing that the most probable false positive scenario was that of a background eclipsing binary, which had a model-dependent probability of $\approx 10^{-5}$. However, this calculation was performed without knowledge of the low-mass stellar companion ($M_B \approx 0.33 M_\odot$). Validated planets have also previously been refuted (e.g., Shporer et al. 2017). We therefore reassessed false positive scenarios in some detail.

As an initial plausibility check, Kepler 1627B contributes 1% to 2% of the total flux observed in the Kepler aperture. For the sake of argument, assume the former value. The observed transit has a depth of $\approx 0.18\%$. A 18% deep eclipse of Kepler 1627B would therefore be needed to produce a signal with the appropriate depth. The shape of the transit signal however requires the impact parameter to be below 0.77 (2- σ); the tertiary transiting the secondary would therefore need to be non-grazing with $R_3/R_2 \approx 0.4$. This yields a contradiction: this scenario requires an ingress and egress phase that each span $\approx 40\%$ of the transit duration (≈ 68 min). The actual measured ingress and egress duration is ≈ 17 min, a factor of four times too short. The combination of Kepler 1627B's

brightness, the transit depth, and the ingress duration therefore disfavor the scenario that Kepler 1627B might host the transit signal.

Beyond this simple test, a line of evidence that effectively confirms the planetary interpretation is that the stellar density implied by the transit duration and orbital period is inconsistent with an eclipsing body around the M-dwarf companion. We find $\rho_* = 2.00 \pm 0.24 \text{ g cm}^{-3}$, while the theoretically expected density for Kepler 1627B is $\approx 4.6 \text{ g cm}^{-3}$ (Table 2; Choi et al. 2016). The transit duration is therefore too long to be explained by a star eclipsing the M dwarf secondary at 10- σ . While the planet might hypothetically still orbit a hidden close and bright companion, this possibility is implausible given i) the lack of secondary lines in the HIRES spectra, ii) the lack of secondary rotation signals in the Kepler photometry, and iii) the proximity of Kepler 1627 to the δ Lyr cluster locus on the Gaia CAMD (Figure 3).

The correlation noted in Section 4.1.3 between the TTVs and the local light curve slope might be an additional line of evidence in support of the planetary interpretation. Unless it is a statistical fluke (a $\approx 5\%$ possibility), then the most likely cause of the correlation is unresolved starspot

crossings (Mazeh et al. 2015). These would only be possible if the planet transits the primary star, which excludes a background eclipsing binary scenario. The correlation would also suggest that the planet’s orbit is prograde. The latter point assumes that the dominant photometric variability is induced by dark spots, and not bright faculae. Given the observed transition of Sun-like stellar variability from spot to faculae-dominated regimes between young and old ages, we expect this latter assumption to be reasonably secure (Shapiro et al. 2016; Montet et al. 2017; Reinhold & Hekker 2020).

A third supporting line of evidence for the planetary interpretation also exists. We observed a transit of Kepler 1627Ab on the night of 2021 Aug 7 simultaneously with Keck/HIRES and MuSCAT3. We scheduled the observations using the ephemeris of Holczer et al. (2016). Although we did not detect the Rossiter-McLaughlin (RM) anomaly, the multi-band MuSCAT3 light curves show that the transit is achromatic (Figure 7). Quantitatively, when we fitted the MuSCAT3 photometry with a model that lets the transit depths vary across each bandpass, we found *griz* depths consistent with the Kepler depth at 0.6, 0.3, 0.3, and 1.1σ respectively. Conditioned on the ephemeris and transit depth from the Kepler data, the MuSCAT3 observations also suggested a transit duration 17.3 ± 4.3 min shorter than the Kepler transits. However, given both the lack of TDVs in the Kepler data and the relatively low signal-to-noise of the MuSCAT3 transit, further photometric follow-up would be necessary to determine whether the transit duration is indeed changing. For our RM analysis, the details are discussed in Appendix C. While the velocities are marginally more consistent with a prograde or polar orbit than a retrograde orbit, the spot-corrected exposure-to-exposure scatter ($\sigma_{RV} \approx 30 \text{ m s}^{-1}$) is comparable to the expected RM anomaly assuming an aligned orbit ($\Delta v_{RM} \approx 20 \text{ m s}^{-1}$). We are therefore not in a position to claim a spectroscopic detection of the RM effect, nor to quantify the stellar obliquity.

5. DISCUSSION & CONCLUSIONS

Kepler 1627Ab provides a new extremum in the ages of the Kepler planets, and opens multiple avenues for further study. Observations of spectroscopic transits at greater precision should yield a measurement of the stellar obliquity, which would confirm or refute the prograde orbital geometry suggested by the TTV-local slope correlation. Separately, transit spectroscopy aimed at detecting atmospheric outflows could yield insight into the evolutionary state of the atmosphere (e.g., Ehrenreich et al. 2015; Spake et al. 2018; Vissapragada et al. 2020). Observations that quantify the

amount of high-energy irradiation incident on the planet would complement these efforts, by helping to clarify the expected outflow rate (e.g., Poppenhaeger et al. 2021). Finally, a challenging but informative quantity to measure would be the planet’s mass. Measured at sufficient precision, for instance through a multi-wavelength radial velocity campaign, the combination of the size, mass, and age would yield constraints on both the planet’s composition and its initial entropy (Owen 2020).

More immediately, the Kepler data may yet contain additional information. For instance, one possible explanation for the transit asymmetry shown in Figure 5 is that of a dusty asymmetric outflow. Dusty outflows are theoretically expected for young mini-Neptunes, and the amplitude of the observed asymmetry is consistent with predictions (Wang & Dai 2019). A second possibility is that the planetary orbit is slightly misaligned from the stellar spin axis, and tends to transit starspot groups at favored stellar latitudes. This geometry would be necessary in order to explain how the starspot crossings could add up coherently. Other possibilities including gravity darkening or TTVs causing the asymmetry are disfavored (see Appendix B).

Beyond the asymmetric transits, Appendix D highlights an additional abnormality in the short-cadence Kepler data, in the arrival time distribution of stellar flares. We encourage its exploration by investigators more versed in the topic than ourselves.

In the context of the transiting planet population, Kepler 1627Ab is among the youngest known (Figure 8). Comparable systems with precise ages include K2-33 (Mann et al. 2016; David et al. 2016), DS Tuc (Benatti et al. 2019; Newton et al. 2019), HIP 67522 (Rizzuto et al. 2020), TOI 837 (Bouma et al. 2020), the two-planet AU Mic (Plavchan et al. 2020; Martioli et al. 2021) and the four-planet V1298 Tau (David et al. 2019). Kepler 1627Ab is one of the smaller planets in this sample ($3.82 \pm 0.16 R_\oplus$), which could be linked to the selection effects imposed by spot-induced photometric variability at very young ages (e.g., Zhou et al. 2021). However, smaller planets could have been detected: the Kepler pipeline’s median completeness extended to $1.6 R_\oplus$ at 10 day orbital periods, and $3.3 R_\oplus$ at 100 days (Burke & Catanzarite 2021). The large size of Kepler 1627Ab relative to most Kepler mini-Neptunes might therefore support a picture in which the typical $5 M_\oplus$ to $10 M_\oplus$ mini-Neptune (Wu 2019) loses a significant fraction of its primordial atmosphere over its first gigayear (Owen & Wu 2013; Ginzburg et al. 2018). **(Added: This of course depends on the mass of Kepler 1627Ab; an alternative explanation for its large size could simply be that it is more mas-**

789 **sive than the typical Kepler mini-Neptune, or
790 that it has an abnormally large envelope to core
791 mass ratio.)**

792 Ultimately, the main advance of this work is a
793 precise measurement of the age of Kepler 1627Ab.
794 This measurement was enabled by identifying the
795 connection of the star to the δ Lyr cluster using
796 Gaia kinematics, and by then using the Gaia color-
797 absolute magnitude diagram and TESS stellar ro-
798 tation periods to verify the cluster's existence. Ta-
799 ble 3 enables similar cross-matches for both known
800 and forthcoming exoplanet systems (e.g., Guerrero
801 et al. 2021). Confirming these candidate associa-
802 tions using independent age indicators is essential
803 because their false positive rates are not known. A
804 related path is to identify new kinematic associa-
805 tions around known exoplanet host stars using po-
806 sitions and tangential velocities from Gaia, and to
807 verify these associations with stellar rotation peri-
808 ods and spectroscopy (e.g., Tofflemire et al. 2021).
809 Each approach seems likely to expand the census
810 of planets with precisely measured ages over the
811 coming years, which will help in deciphering the
812 early stages of exoplanet evolution.

ACKNOWLEDGMENTS

813 The authors are grateful to J. Winn, J. Spake,
814 A. Howard, and T. David for illuminating dis-
815 cussions and suggestions, and to R. Kerr for pro-
816 viding us with the Kerr et al. (2021) mem-
817 bership list prior to its publication. The authors are
818 also grateful to K. Collins for helping resolve the
819 scheduling conflict that would have otherwise pre-
820 vented the MuSCAT3 observations. L.G.B. ac-
821 knowledges support from a Charlotte Elizabeth
822 Procter Fellowship from Princeton University, as
823 well as from the TESS GI Program (NASA grants
824 80NSSC19K0386 and 80NSSC19K1728) and the
825 Heising-Simons Foundation (51 Pegasi b Fellow-
826 ship). Keck/NIRC2 imaging was acquired by pro-
827 gram 2015A/N301N2L (PI: A. Kraus). In addition,
828 this paper is based in part on observations made
829 with the MuSCAT3 instrument, developed by the
830 Astrobiology Center and under financial support by
831 JSPS KAKENHI (JP18H05439) and JST PRESTO
832 (JPMJPR1775), at Faulkes Telescope North on
833 Maui, HI, operated by the Las Cumbres Observa-
834 tory. This work is partly supported by JSPS KAK-
835 ENHI Grant Numbers 22000005, JP15H02063,
836 JP17H04574, JP18H05439, JP18H05442, JST
837 PRESTO Grant Number JPMJPR1775, the Astro-
838 biology Center of National Institutes of Natural
839 Sciences (NINS) (Grant Number AB031010). This
840 paper also includes data collected by the TESS
841 mission, which are publicly available from the

842 Mikulski Archive for Space Telescopes (MAST).
843 Funding for the TESS mission is provided by
844 NASA's Science Mission directorate. We thank
845 the TESS Architects (G. Ricker, R. Vanderspek,
846 D. Latham, S. Seager, J. Jenkins) and the many
847 TESS team members for their efforts to make the
848 mission a continued success. Finally, this research
849 has made use of the Keck Observatory Archive
850 (KOA), which is operated by the W. M. Keck Ob-
851 servatory and the NASA Exoplanet Science Insti-
852 tute (NExScI), under contract with the National
853 Aeronautics and Space Administration. We also
854 thank the Keck Observatory staff for their support
855 of HIRES and remote observing. We recognize
856 the importance that the summit of Maunakea has
857 within the indigenous Hawaiian community, and
858 are deeply grateful to have the opportunity to con-
859 duct observations from this mountain.

860 **Software:** *altaipony* (Ilin et al. 2021),
861 *astrobase* (Bhatti et al. 2018), *astropy* (As-
862 *trophy Collaboration* et al. 2018), *astroquery*
863 (Ginsburg et al. 2018), *corner* (Foreman-Mackey
864 2016), *exoplanet* (Foreman-Mackey et al.
865 2020), and its dependencies (Agol et al. 2020; Kip-
866 ping 2013; Luger et al. 2019; Theano Develop-
867 ment Team 2016), *PyMC3* (Salvatier et al. 2016),
868 *scipy* (Jones et al. 2001), *TESS-point* (Burke
869 et al. 2020), *wotan* (Hippke et al. 2019).

870 **Facilities:** *Astrometry:* Gaia (Gaia Col-
871 laboration et al. 2018b, 2021a). *Imaging:*
872 Second Generation Digitized Sky Survey.
873 Keck:II (NIRC2; [www2.keck.hawaii.edu/inst/
nirc2](http://www2.keck.hawaii.edu/inst/nirc2)). Gemini:North ('Alopeke; Scott et al. 2018,
875 2021). *Spectroscopy:* Keck:I (HIRES; Vogt et al.
876 1994). *Photometry:* Kepler (Borucki et al. 2010),
877 MuSCAT3 (Narita et al. 2020), TESS (Ricker et al.
878 2015).

Table 1. Literature and Measured Properties for Kepler 1627

Primary Star			
TIC 120105470 GAIADR2 [†] 2103737241426734336			
Parameter	Description	Value	Source
$\alpha_{J2015.5}$	Right Ascension (hh:mm:ss)	18:56:13.6	1
$\delta_{J2015.5}$	Declination (dd:mm:ss)	+41:34:36.22	1
V	Johnson V mag.	13.11 \pm 0.08	2
G	Gaia G mag.	13.02 \pm 0.02	1
G_{BP}	Gaia BP mag.	13.43 \pm 0.02	1
G_{RP}	Gaia RP mag.	12.44 \pm 0.02	1
T	TESS T mag.	12.53 \pm 0.02	2
J	2MASS J mag.	11.69 \pm 0.02	3
H	2MASS H mag.	11.30 \pm 0.02	3
K _S	2MASS K _S mag.	11.19 \pm 0.02	3
π	Gaia EDR3 parallax (mas)	3.009 \pm 0.032	1
d	Distance (pc)	329.5 \pm 3.5	1, 4
μ_α	Gaia EDR3 proper motion	1.716 \pm 0.034	1
	in RA (mas yr ⁻¹)		
μ_δ	Gaia EDR3 proper motion	-1.315 \pm 0.034	1
	in DEC (mas yr ⁻¹)		
RUWE	Gaia EDR3 renormalized	2.899	1
	unit weight error		
RV	Systemic radial velocity (km s ⁻¹)	-16.7 \pm 1.0	5
Spec. Type	Spectral Type	G8V	5
$v \sin i_*$	Rotational velocity* (km s ⁻¹)	18.9 \pm 1.0	5
Li EW	6708Å Equiv. Width (mÅ)	235 ⁺⁵ ₋₇	5
T_{eff}	Effective Temperature (K)	5505 \pm 60	6
$\log g_*$	Surface Gravity (cgs)	4.53 \pm 0.05	6
R_*	Stellar radius (R_\odot)	0.881 \pm 0.018	6
M_*	Stellar mass (R_\odot)	0.953 \pm 0.019	6
Av	Interstellar reddening (mag)	0.2 \pm 0.1	6
[Fe/H]	Metallicity	0.1 \pm 0.1	6
P_{rot}	Rotation period (d)	2.642 \pm 0.042	7
Age	Adopted stellar age (Myr)	38 ⁺⁶ ₋₅	8
Δm_{832}	Mag difference ('Alopeke 832 nm)	3.14 \pm 0.15	9
θ_B	Position angle (deg)	92 \pm 1	9
ρ_B	Apparent separation of	0.164 \pm 0.002	9
	primary and secondary (as)		
ρ_B	Apparent separation of	53 \pm 4	1, 4, 9
	primary and secondary (AU)		
$\Delta m_{K'}$	Mag difference (NIRC2 K')	2.37 \pm 0.02	10
θ_B	Position angle (deg)	95.9 \pm 0.5	10
ρ_B	Apparent separation of	0.1739 \pm 0.0010	10
	primary and secondary (as)		

NOTE—[†] The GAIADR2 and GAIAEDR3 identifiers for Kepler 1627A are identical. The secondary is not resolved in the Gaia point source catalog. * Given only $v \sin i$ and $2\pi R_*/P_{\text{rot}}$, $\cos i = 0.11^{+0.11}_{-0.08}$. Provenances are: ¹Gaia Collaboration et al. (2021a), ²Stassun et al. (2019), ³Skrutskie et al. (2006), ⁴Lindgren et al. (2021), ⁵HIRESS spectra and Yee et al. (2017), ⁶Cluster isochrone (MIST adopted; PARSEC compared for quoted uncertainty), ⁷Kepler light curve, ⁸Pre-main-sequence CAMD interpolation (Section 2.2.1), ⁹'Alopeke imaging 2021 June 24 (Scott et al. 2021), ¹⁰NIRC2 imaging 2015 July 22, using the Yelda et al. (2010) optical distortion solution to convert pixel-space relative positions to on-sky relative astrometry. The “discrepancy” between the two imaging epochs likely indicates orbital motion.

Table 2. Priors and Posteriors for Model Fitted to the Long Cadence Kepler 1627Ab Light Curve.

Param.	Unit	Prior	Median	Mean	Std. Dev.	3%	97%	ESS	$\hat{R} - 1$
<i>Sampled</i>									
P	d	$\mathcal{N}(7.20281; 0.01000)$	7.2028038	7.2028038	0.0000073	7.2027895	7.2028168	7464	3.9e-04
$t_0^{(1)}$	d	$\mathcal{N}(120.79053; 0.02000)$	120.7904317	120.7904254	0.0009570	120.7886377	120.7921911	3880	2.0e-03
$\log \delta$	—	$\mathcal{N}(-6.3200; 2.0000)$	-6.3430	-6.3434	0.0354	-6.4094	-6.2767	6457	3.0e-04
$b^{(2)}$	—	$\mathcal{U}(0.000; 1.000)$	0.4669	0.4442	0.2025	0.0662	0.8133	1154	1.6e-03
u_1	—	Kipping (2013)	0.271	0.294	0.190	0.000	0.628	3604	1.5e-03
u_2	—	Kipping (2013)	0.414	0.377	0.326	-0.240	0.902	3209	1.4e-03
R_*	R_{\odot}	$\mathcal{N}(0.881; 0.018)$	0.881	0.881	0.018	0.847	0.915	8977	3.1e-04
$\log g$	cgs	$\mathcal{N}(4.530; 0.050)$	4.532	4.533	0.051	4.435	4.627	6844	1.6e-03
$\langle f \rangle$	—	$\mathcal{N}(0.000; 0.100)$	-0.0003	-0.0003	0.0001	-0.0005	-0.0000	8328	1.1e-03
$e^{(3)}$	—	Van Eylen et al. (2019)	0.154	0.186	0.152	0.000	0.459	1867	2.0e-03
ω	rad	$\mathcal{U}(0.000; 6.283)$	0.055	0.029	1.845	-3.139	2.850	3557	8.6e-05
$\log \sigma_f$	—	$\mathcal{N}(\log \langle \sigma_f \rangle; 2.000)$	-8.035	-8.035	0.008	-8.049	-8.021	9590	3.9e-04
σ_{rot}	d^{-1}	InvGamma(1.000; 5.000)	0.070	0.070	0.001	0.068	0.072	9419	1.4e-03
$\log P_{\text{rot}}$	log(d)	$\mathcal{N}(0.958; 0.020)$	0.978	0.978	0.001	0.975	0.980	8320	2.2e-04
$\log Q_0$	—	$\mathcal{N}(0.000; 2.000)$	-0.327	-0.326	0.043	-0.407	-0.246	9659	2.7e-04
$\log dQ$	—	$\mathcal{N}(0.000; 2.000)$	7.697	7.698	0.103	7.511	7.899	5824	3.7e-04
f	—	$\mathcal{U}(0.010; 1.000)$	0.01006	0.01009	0.00009	0.01000	0.01025	4645	4.0e-04
<i>Derived</i>									
δ	—	—	0.001759	0.001759	0.000062	0.001641	0.001875	6457	3.0e-04
R_p/R_*	—	—	0.039	0.039	0.001	0.037	0.042	1811	1.1e-03
ρ_*	g cm^{-3}	—	1.990	2.004	0.240	1.570	2.461	6905	2.1e-03
$R_p^{(4)}$	R_{Jup}	—	0.337	0.338	0.014	0.314	0.367	2311	1.0e-03
$R_p^{(4)}$	R_{Earth}	—	3.777	3.789	0.157	3.52	4.114	2311	1.0e-03
a/R_*	—	—	17.606	17.619	0.702	16.277	18.906	6905	2.1e-03
$\cos i$	—	—	0.027	0.025	0.010	0.004	0.040	1312	1.2e-03
T_{14}	hr	—	2.841	2.843	0.060	2.734	2.958	3199	3.6e-04
T_{13}	hr	—	2.555	2.539	0.094	2.360	2.692	1960	1.4e-03

NOTE— ESS refers to the number of effective samples. \hat{R} is the Gelman-Rubin convergence diagnostic. Logarithms in this table are base-e. \mathcal{U} denotes a uniform distribution, and \mathcal{N} a normal distribution. (1) The ephemeris is in units of BJDTDB - 2454833. (2) Although $\mathcal{U}(0, 1 + R_p/R_*)$ is formally correct, for this model we assumed a non-grazing transit to enable sampling in $\log \delta$. (3) The eccentricity vectors are sampled in the $(e \cos \omega, e \sin \omega)$ plane. (4) The true planet size is a factor of $((F_1 + F_2)/F_1)^{1/2}$ larger than that from the fit because of dilution from Kepler 1627B, where F_1 is the flux from the primary, and F_2 is that from the secondary; the mean and standard deviation of $R_p = 3.817 \pm 0.158 R_{\oplus}$ quoted in the text includes this correction, assuming $(F_1 + F_2)/F_1 \approx 1.015$.

Table 3. Young, Age-dated, and Age-dateable Stars Within the Nearest Few Kiloparsecs.

Parameter	Example Value	Description
source_id	1709456705329541504	Gaia DR2 source identifier.
ra	247.826	Gaia DR2 right ascension [deg].
dec	79.789	Gaia DR2 declination [deg].
parallax	35.345	Gaia DR2 parallax [mas].
parallax_error	0.028	Gaia DR2 parallax uncertainty [mas].
pmra	94.884	Gaia DR2 proper motion $\mu_{\alpha} \cos \delta$ [mas yr $^{-1}$].
pmdec	-86.971	Gaia DR2 proper motion μ_{δ} [mas yr $^{-1}$].
phot_g_mean_mag	6.85	Gaia DR2 G magnitude.
phot_bp_mean_mag	6.409	Gaia DR2 G_{BP} magnitude.
phot_rp_mean_mag	7.189	Gaia DR2 G_{RP} magnitude.
cluster	NASAExoArchive_ps_20210506.Uma,IR_excess	Comma-separated cluster or group name.
age	9.48,nan,nan	Comma-separated logarithm (base-10) of reported ^a age in years.
mean_age	9.48	Mean (ignoring NaNs) of age column.
reference_id	NASAExoArchive_ps_20210506,Ujjwal2020,CottenSong2016	Comma-separated provenance of group membership.
reference_bibcode	2013PASP..125..989A,2020AJ....159..166U,2016ApJS..225..15C	ADS bibcode corresponding to reference_id.

NOTE— Table 3 is published in its entirety in a machine-readable format. This table is a concatenation of the studies listed in Table 4. One entry is shown for guidance regarding form and content. In this particular example, the star has a cold Jupiter on a 16 year orbit, HD 150706b (Boisse et al. 2012). An infrared excess has been reported (Cotten & Song 2016), and the star was identified by Ujjwal et al. (2020) as a candidate UMa moving group member (≈ 400 Myr; Mann et al. 2020). The star's RV activity and TESS rotation period corroborate its youth.

Table 4. Provenances of Young and Age-dateable Stars.

Reference	N_{Gaia}	N_{Age}	$N_{G_{\text{RP}} < 16}$
Kounkel et al. (2020)	987376	987376	775363
Cantat-Gaudin & Anders (2020)	433669	412671	269566
Cantat-Gaudin et al. (2018)	399654	381837	246067
Kounkel & Covey (2019)	288370	288370	229506
Cantat-Gaudin et al. (2020)	233369	227370	183974
Zari et al. (2018) UMS	86102	0	86102
Wenger et al. (2000) Y*?	61432	0	45076
Zari et al. (2018) PMS	43719	0	38435
Gaia Collaboration et al. (2018a) $d > 250 \text{ pc}$	35506	31182	18830
Castro-Ginard et al. (2020)	33635	24834	31662
Kerr et al. (2021)	30518	25324	27307
Wenger et al. (2000) Y*○	28406	0	16205
Villa Vélez et al. (2018)	14459	14459	13866
Cantat-Gaudin et al. (2019)	11843	11843	9246
Damiani et al. (2019) PMS	10839	10839	9901
Oh et al. (2017)	10379	0	10370
Meingast et al. (2021)	7925	7925	5878
Wenger et al. (2000) pMS*	5901	0	3006
Gaia Collaboration et al. (2018a) $d < 250 \text{ pc}$	5378	817	3968
Kounkel et al. (2018)	5207	3740	5207
Ratzenböck et al. (2020)	4269	4269	2662
Wenger et al. (2000) TT*	4022	0	3344
Damiani et al. (2019) UMS	3598	3598	3598
Rizzuto et al. (2017)	3294	3294	2757
Akeson et al. (2013)	3107	868	3098
Tian (2020)	1989	1989	1394
Goldman et al. (2018)	1844	1844	1783
Cotten & Song (2016)	1695	0	1693
Gagné et al. (2018b)	1429	0	1389
Röser & Schilbach (2020) Psc-Eri	1387	1387	1107
Röser & Schilbach (2020) Pleiades	1245	1245	1019
Wenger et al. (2000) TT?	1198	0	853
Gagné & Faherty (2018)	914	0	913
Pavlidou et al. (2021)	913	913	504
Gagné et al. (2018a)	692	0	692
Ujjwal et al. (2020)	563	0	563
Gagné et al. (2020)	566	566	351
Esplin & Luhman (2019)	377	443	296
Roccatagliata et al. (2020)	283	283	232
Meingast & Alves (2019)	238	238	238
Fürnkranz et al. (2019) Coma-Ber	214	214	213
Fürnkranz et al. (2019) Neighbor Group	177	177	167
Kraus et al. (2014)	145	145	145

NOTE— Table 4 describes the provenances for the young and age-dateable stars in Table 3. N_{Gaia} : number of Gaia stars we parsed from the literature source. N_{Age} : number of stars in the literature source with ages reported. $N_{G_{\text{RP}} < 16}$: number of Gaia stars we parsed from the literature source with either $G_{\text{RP}} < 16$, or a parallax S/N exceeding 5 and a distance closer than 100 pc. The latter criterion included a few hundred white dwarfs that would have otherwise been neglected. Some studies are listed multiple times if they contain multiple tables. Wenger et al. (2000) refers to the SIMBAD database.

REFERENCES

- 879 Agol, E., Luger, R., & Foreman-Mackey, D. 2020, *AJ*,
 880 159, 123
- 881 Akeson, R. L., Chen, X., Ciardi, D., et al. 2013, *PASP*,
 882 125, 989
- 883 Astropy Collaboration, Price-Whelan, A. M., Sipőcz,
 884 B. M., et al. 2018, *AJ*, 156, 123
- 885 Baraffe, I., Homeier, D., Allard, F., & Chabrier, G.
 886 2015, *A&A*, 577, A42
- 887 Beaumont, C., Robitaille, T., Borkin, M., & Goodman,
 888 A. 2014, glueviz v0.4: multidimensional data
 889 exploration
- 890 Benatti, S., Nardiello, D., Malavolta, L., et al. 2019,
 891 *A&A*, 630, A81
- 892 Berger, T. A., Howard, A. W., & Boesgaard, A. M.
 893 2018, *ApJ*, 855, 115
- 894 Berger, T. A., Huber, D., Gaidos, E., & van Saders, J. L.
 895 2018, *ApJ*, 866, 99
- 896 Bhatti, W., Bouma, L. G., & Wallace, J. 2018,
 897 astrobase,
 898 <https://doi.org/10.5281/zenodo.1469822>
- 899 Boisse, I., Pepe, F., Perrier, C., et al. 2012, *A&A*, 545,
 900 A55
- 901 Borucki, W. J., Koch, D., Basri, G., et al. 2010, *Science*,
 902 327, 977
- 903 Bossini, D., Vallenari, A., Bragaglia, A., et al. 2019,
 904 *A&A*, 623, A108
- 905 Bouma, L. G., Curtis, J. L., Hartman, J. D., Winn, J. N.,
 906 & Bakos, G. A. 2021, arXiv:2107.08050 [astro-ph]
- 907 Bouma, L. G., Hartman, J. D., Bhatti, W., Winn, J. N.,
 908 & Bakos, G. Á. 2019, *ApJS*, 245, 13
- 909 Bouma, L. G., Hartman, J. D., Brahm, R., et al. 2020,
 910 *AJ*, 160, 239
- 911 Bressan, A., Marigo, P., Girardi, L., et al. 2012,
 912 *MNRAS*, 427, 127
- 913 Burke, C., & Catanzarite, J. 2021, KeplerPORTS:
 914 Kepler Planet Occurrence Rate Tools
- 915 Burke, C. J., Levine, A., Fausnaugh, M., et al. 2020,
 916 TESS-Point: High precision TESS pointing tool,
 917 Astrophysics Source Code Library, ascl:2003.001
- 918 Cantat-Gaudin, T., & Anders, F. 2020, *A&A*, 633, A99
- 919 Cantat-Gaudin, T., Jordi, C., Vallenari, A., et al. 2018,
 920 *A&A*, 618, A93
- 921 Cantat-Gaudin, T., Jordi, C., Wright, N. J., et al. 2019,
 922 *A&A*, 626, A17
- 923 Cantat-Gaudin, T., Anders, F., Castro-Ginard, A., et al.
 924 2020, *A&A*, 640, A1
- 925 Capitanio, L., Lallement, R., Vergely, J. L., Elyajouri,
 926 M., & Monreal-Ibero, A. 2017, *A&A*, 606, A65
- 927 Castro-Ginard, A., Jordi, C., Luri, X., et al. 2020, *A&A*,
 928 635, A45
- 929 Choi, J., Dotter, A., Conroy, C., et al. 2016, *ApJ*, 823,
 930 102
- 931 Claret, A., & Bloemen, S. 2011, *A&A*, 529, A75
- 932 Cotten, T. H., & Song, I. 2016, *ApJS*, 225, 15
- 933 Dahm, S. E. 2015, *ApJ*, 813, 108
- 934 Dai, F., Winn, J. N., Berta-Thompson, Z.,
 935 Sanchis-Ojeda, R., & Albrecht, S. 2018, *AJ*, 155, 177
- 936 Damiani, F., Prisinzano, L., Pillitteri, I., Micela, G., &
 937 Sciortino, S. 2019, *A&A*, 623, A112
- 938 Davenport, J. R. A. 2016, *ApJ*, 829, 23
- 939 Davenport, J. R. A., Hawley, S. L., Hebb, L., et al.
 940 2014, *ApJ*, 797, 122
- 941 David, T., Hillenbrand, L., & Petigura, E. 2016, *Nature*,
 942 534, 658
- 943 David, T. J., & Hillenbrand, L. A. 2015, *ApJ*, 804, 146
- 944 David, T. J., Petigura, E. A., Luger, R., et al. 2019,
 945 *ApJL*, 885, L12
- 946 David, T. J., Contardo, G., Sandoval, A., et al. 2021, *AJ*,
 947 161, 265
- 948 Dias, W. S., Monteiro, H., Caetano, T. C., et al. 2014,
 949 *A&A*, 564, A79
- 950 Dobbie, P. D., Lodieu, N., & Sharp, R. G. 2010,
 951 *MNRAS*, 409, 1002
- 952 Douglas, S. T., Agüeros, M. A., Covey, K. R., & Kraus,
 953 A. 2017, *ApJ*, 842, 83
- 954 Douglas, S. T., Pérez Chávez, J., Cargile, P. A., et al.
 955 2021, [10.5281/zenodo.5131306](https://doi.org/10.5281/zenodo.5131306)
- 956 Eggen, O. J. 1968, *ApJ*, 152, 77
- 957 Ehrenreich, D., Bourrier, V., Wheatley, P. J., et al. 2015,
 958 *Nature*, 522, 459
- 959 Esplin, T. L., & Luhman, K. L. 2019, *AJ*, 158, 54
- 960 Feinstein, A. D., Montet, B. T., Johnson, M. C., et al.
 961 2021, arXiv:2107.01213 [astro-ph]
- 962 Foreman-Mackey, D. 2016, *Journal of Open Source
 963 Software*, 1, 24
- 964 Foreman-Mackey, D., Czekala, I., Luger, R., et al. 2020,
 965 exoplanet-dev/exoplanet v0.2.6
- 966 Fulton, B. J., Petigura, E. A., Howard, A. W., et al.
 967 2017, *AJ*, 154, 109
- 968 Fürnkranz, V., Meingast, S., & Alves, J. 2019, *A&A*,
 969 624, L11
- 970 Gagné, J., David, T. J., Mamajek, E. E., et al. 2020,
 971 *ApJ*, 903, 96
- 972 Gagné, J., & Faherty, J. K. 2018, *ApJ*, 862, 138
- 973 Gagné, J., Roy-Loubier, O., Faherty, J. K., Doyon, R.,
 974 & Malo, L. 2018a, *ApJ*, 860, 43

- 975 Gagné, J., Mamajek, E. E., Malo, L., et al. 2018b, *ApJ*,
976 **856**, 23
- 977 Gagné, J., David, T. J., Mamajek, E. E., et al. 2020,
978 *ApJ*, **903**, 96
- 979 Gaia Collaboration, Babusiaux, C., van Leeuwen, F.,
980 et al. 2018a, *A&A*, **616**, A10
- 981 Gaia Collaboration, Brown, A. G. A., Vallenari, A.,
982 et al. 2018b, *A&A*, **616**, A1
- 983 —. 2021a, *A&A*, **649**, A1
- 984 Gaia Collaboration, Smart, R. L., Sarro, L. M., et al.
985 2021b, *A&A*, **649**, A6
- 986 Gelman, A., & Rubin, D. B. 1992, *Statistical Science*, **7**,
987 457, publisher: Institute of Mathematical Statistics
- 988 Gibson, S. R., Howard, A. W., Marcy, G. W., et al. 2016,
989 in *SPIE Conference Series*, Vol. 9908, *Ground-based*
990 and *Airborne Instrumentation for Astronomy VI*, ed.
991 C. J. Evans, L. Simard, & H. Takami, 990870
- 992 Gillen, E., Briegal, J. T., Hodgkin, S. T., et al. 2020,
993 *MNRAS*, **492**, 1008
- 994 Ginsburg, A., Sipocz, B., Madhura Parikh, et al. 2018,
995 *Astropy/Astroquery: V0.3.7 Release*
- 996 Ginzburg, S., Schlichting, H. E., & Sari, R. 2018,
997 *MNRAS*, **476**, 759
- 998 Goldman, B., Röser, S., Schilbach, E., Moór, A. C., &
999 Henning, T. 2018, *ApJ*, **868**, 32
- 1000 Guerrero, N. M., Seager, S., Huang, C. X., et al. 2021,
1001 *ApJS*, **254**, 39
- 1002 Günther, M. N., Zhan, Z., Seager, S., et al. 2020, *AJ*,
1003 **159**, 60
- 1004 Hattori, S., Foreman-Mackey, D., Hogg, D. W., et al.
1005 2021, arXiv e-prints, arXiv:2106.15063
- 1006 Hippke, M., David, T. J., Mulders, G. D., & Heller, R.
1007 2019, *AJ*, **158**, 143
- 1008 Hirano, T., Suto, Y., Taruya, A., et al. 2010, *ApJ*, **709**,
1009 458
- 1010 Hirano, T., Suto, Y., Winn, J. N., et al. 2011, *ApJ*, **742**,
1011 69
- 1012 Hoffman, M. D., & Gelman, A. 2014, *Journal of
1013 Machine Learning Research*, **15**, 1593
- 1014 Holczer, T., Shporer, A., Mazeh, T., et al. 2015, *ApJ*,
1015 **807**, 170
- 1016 Holczer, T., Mazeh, T., Nachmani, G., et al. 2016,
1017 *ApJS*, **225**, 9
- 1018 Howard, A. W., Johnson, J. A., Marcy, G. W., et al.
1019 2010, *ApJ*, **721**, 1467
- 1020 Howell, S. B., Everett, M. E., Sherry, W., Horch, E., &
1021 Ciardi, D. R. 2011, *AJ*, **142**, 19
- 1022 Ikoma, M., & Hori, Y. 2012, *ApJ*, **753**, 66
- 1023 Ilin, E., Schmidt, S. J., Poppenhöger, K., et al. 2021,
1024 *A&A*, **645**, A42
- 1025 Jones, E., Oliphant, T., Peterson, P., et al. 2001, Open
1026 source scientific tools for Python
- 1027 Kerr, R. M. P., Rizzato, A. C., Kraus, A. L., & Offner,
1028 S. S. R. 2021, *ApJ*, **917**, 23
- 1029 Kharchenko, N. V., Piskunov, A. E., Schilbach, E.,
1030 Röser, S., & Scholz, R.-D. 2013, *A&A*, **558**, A53
- 1031 Kipping, D. M. 2010, *MNRAS*, **408**, 1758
- 1032 Kipping, D. M. 2013, *MNRAS*, **435**, 2152
- 1033 Kite, E. S., Fegley, Jr., B., Schaefer, L., & Ford, E. B.
1034 2020, *ApJ*, **891**, 111
- 1035 Klein, B., & Donati, J.-F. 2020, *MNRAS*, **493**, L92
- 1036 Kounkel, M., & Covey, K. 2019, *AJ*, **158**, 122
- 1037 Kounkel, M., Covey, K., & Stassun, K. G. 2020, *AJ*,
1038 **160**, 279
- 1039 Kounkel, M., Covey, K., Suárez, G., et al. 2018, *AJ*,
1040 **156**, 84
- 1041 Kounkel, M., Covey, K., Suárez, G., et al. 2018, *AJ*,
1042 **156**, 84
- 1043 Kraus, A. L., Ireland, M. J., Huber, D., Mann, A. W., &
1044 Dupuy, T. J. 2016, *AJ*, **152**, 8
- 1045 Kraus, A. L., Shkolnik, E. L., Allers, K. N., & Liu,
1046 M. C. 2014, *AJ*, **147**, 146
- 1047 Lallement, R., Capitanio, L., Ruiz-Dern, L., et al. 2018,
1048 *A&A*, **616**, A132
- 1049 Lindegren, L., Bastian, U., Biermann, M., et al. 2021,
1050 *A&A*, **649**, A4
- 1051 Lomb, N. R. 1976, *Astrophysics and Space Science*, **39**,
1052 447
- 1053 Lopez, E. D., Fortney, J. J., & Miller, N. 2012, *ApJ*,
1054 **761**, 59
- 1055 Luger, R., Agol, E., Foreman-Mackey, D., et al. 2019,
1056 *AJ*, **157**, 64
- 1057 Mann, A. W., Newton, E. R., Rizzato, A. C., et al. 2016,
1058 *AJ*, **152**, 61
- 1059 Mann, A. W., Johnson, M. C., Vanderburg, A., et al.
1060 2020, *AJ*, **160**, 179
- 1061 Martioli, E., Hébrard, G., Correia, A. C. M., Laskar, J.,
1062 & Lecavelier des Etangs, A. 2021, *A&A*, **649**, A177
- 1063 Masuda, K. 2015, *ApJ*, **805**, 28
- 1064 Mazeh, T., Holczer, T., & Shporer, A. 2015, *ApJ*, **800**,
1065 142
- 1066 McCann, J., Murray-Clay, R. A., Kratter, K., &
1067 Krumholz, M. R. 2019, *ApJ*, **873**, 89
- 1068 McKinney, W. 2010, in *Proceedings of the 9th Python
1069 in Science Conference*, ed. S. van der Walt &
1070 J. Millman, 51
- 1071 McQuillan, A., Mazeh, T., & Aigrain, S. 2014, *ApJS*,
1072 **211**, 24
- 1073 Meibom, S., Mathieu, R. D., & Stassun, K. G. 2007,
1074 *ApJL*, **665**, L155

- 1075 Meibom, S., Barnes, S. A., Latham, D. W., et al. 2011,
 1076 *ApJL*, **733**, L9
- 1077 Meibom, S., Torres, G., Fressin, F., et al. 2013, *Nature*,
 1078 **499**, 55
- 1079 Meingast, S., & Alves, J. 2019, *A&A*, **621**, L3
- 1080 Meingast, S., Alves, J., & Rottensteiner, A. 2021, *A&A*,
 1081 **645**, A84
- 1082 Montet, B. T., Tovar, G., & Foreman-Mackey, D. 2017,
 1083 *ApJ*, **851**, 116
- 1084 Montet, B. T., Feinstein, A. D., Luger, R., et al. 2020,
 1085 *AJ*, **159**, 112
- 1086 Morris, B. M. 2020, *ApJ*, **893**, 67
- 1087 Morton, T. D., Bryson, S. T., Coughlin, J. L., et al.
 1088 2016, *ApJ*, **822**, 86
- 1089 Narita, N., Fukui, A., Yamamoto, T., et al. 2020, in
 1090 *SPIE Conference Series*, 114475K
- 1091 Newton, E. R., Mann, A. W., Tofflemire, B. M., et al.
 1092 2019, *ApJ*, **880**, L17
- 1093 Oh, S., Price-Whelan, A. M., Hogg, D. W., Morton,
 1094 T. D., & Spergel, D. N. 2017, *AJ*, **153**, 257
- 1095 Owen, J. E. 2020, *MNRAS*, **498**, 5030
- 1096 Owen, J. E., & Wu, Y. 2013, *ApJ*, **775**, 105
 1097 —. 2016, *ApJ*, **817**, 107
- 1098 Palle, E., Oshagh, M., Casasayas-Barris, N., et al. 2020,
 1099 *A&A*, **643**, 25
- 1100 Pavlidou, T., Scholz, A., & Teixeira, P. S. 2021,
 1101 *MNRAS*, **503**, 3232
- 1102 Pecaut, M. J., & Mamajek, E. E. 2013, *ApJS*, **208**, 9
- 1103 Pecaut, M. J., & Mamajek, E. E. 2016, *MNRAS*, **461**,
 1104 794
- 1105 Plavchan, P., Barclay, T., Gagné, J., et al. 2020, *Nature*,
 1106 **582**, 497
- 1107 Poppenhaeger, K., Ketzer, L., & Mallonn, M. 2021,
 1108 *MNRAS*, **500**, 4560
- 1109 Randich, S., Tognelli, E., Jackson, R., et al. 2018, *A&A*,
 1110 **612**, A99
- 1111 Ratzenböck, S., Meingast, S., Alves, J., Möller, T., &
 1112 Bomze, I. 2020, *A&A*, **639**, A64
- 1113 Rebull, L. M., Stauffer, J. R., Bouvier, J., et al. 2016,
 1114 *AJ*, **152**, 113
- 1115 Reinhold, T., & Hekker, S. 2020, *A&A*, **635**, A43
- 1116 Ricker, G. R., Winn, J. N., Vanderspek, R., et al. 2015,
 1117 *JATIS*, **1**, 014003
- 1118 Rizzuto, A. C., Mann, A. W., Vanderburg, A., Kraus,
 1119 A. L., & Covey, K. R. 2017, *AJ*, **154**, 224
- 1120 Rizzuto, A. C., Newton, E. R., Mann, A. W., et al. 2020,
 1121 *AJ*, **160**, 33
- 1122 Roccatagliata, V., Franciosini, E., Sacco, G. G.,
 1123 Randich, S., & Sicilia-Aguilar, A. 2020, *A&A*, **638**,
 1124 A85
- 1125 Roettenbacher, R. M., Monnier, J. D., Korhonen, H.,
 1126 et al. 2017, *ApJ*, **849**, 120
- 1127 Röser, S., & Schilbach, E. 2020, *A&A*, **638**, A9
- 1128 Salvatier, J., Wiecki, T. V., & Fonnesbeck, C. 2016,
 1129 PyMC3: Python probabilistic programming
 1130 framework
- 1131 Scargle, J. D. 1982, *ApJ*, **263**, 835
- 1132 Scott, N. J., Howell, S. B., Horch, E. P., & Everett,
 1133 M. E. 2018, *PASP*, **130**, 054502
- 1134 Scott, N. J., Howell, S. B., Gnilka, C. L., et al. 2021,
 1135 *Frontiers in Astronomy and Space Sciences*, **8**, 138
- 1136 Seifahrt, A., Stürmer, J., Bean, J. L., & Schwab, C.
 1137 2018, in *SPIE Conference Series*, Vol. 10702,
 1138 *Ground-based and Airborne Instrumentation for
 1139 Astronomy VII*, ed. C. J. Evans, L. Simard, &
 1140 H. Takami, 107026D
- 1141 Shapiro, A. I., Solanki, S. K., Krivova, N. A., Yeo,
 1142 K. L., & Schmutz, W. K. 2016, *A&A*, **589**, A46
- 1143 Shporer, A., Zhou, G., Vanderburg, A., et al. 2017,
 1144 *ApJL*, **847**, L18
- 1145 Skrutskie, M. F., Cutri, R. M., Stiening, R., et al. 2006,
 1146 *AJ*, **131**, 1163
- 1147 Smith, J. C., Morris, R. L., Jenkins, J. M., et al. 2016,
 1148 *PASP*, **128**, 124501
- 1149 Smith, J. C., Stumpe, M. C., Jenkins, J. M., et al. 2017,
 1150 *Kepler Science Document*, 8
- 1151 Soderblom, D. R., Hillenbrand, L. A., Jeffries, R. D.,
 1152 Mamajek, E. E., & Naylor, T. 2014, *Protostars and
 1153 Planets VI*, 219
- 1154 Spake, J. J., Sing, D. K., Evans, T. M., et al. 2018,
 1155 *Nature*, **557**, 68
- 1156 Stassun, K. G., Oelkers, R. J., Paegert, M., et al. 2019,
 1157 *AJ*, **158**, 138
- 1158 Stauffer, J., Rebull, L., Bouvier, J., et al. 2016, *AJ*, **152**,
 1159 115
- 1160 Stauffer, J. R., Hartmann, L. W., Prosser, C. F., et al.
 1161 1997, *ApJ*, **479**, 776
- 1162 Stefansson, G., Mahadevan, S., Maney, M., et al. 2020,
 1163 *AJ*, **160**, 192
- 1164 Stephenson, C. B. 1959, *PASP*, **71**, 145
- 1165 Strassmeier, K. G. 2009, *Astronomy and Astrophysics
 1166 Review*, **17**, 251
- 1167 Tenenbaum, P., Christiansen, J. L., Jenkins, J. M., et al.
 1168 2012, *ApJS*, **199**, 24
- 1169 Theano Development Team. 2016, *arXiv e-prints*,
 1170 [abs/1605.02688](https://arxiv.org/abs/1605.02688)
- 1171 Thompson, S. E., Coughlin, J. L., Hoffman, K., et al.
 1172 2018, *ApJS*, **235**, 38
- 1173 Tian, H.-J. 2020, *ApJ*, **904**, 196
- 1174 Tofflemire, B. M., Rizzuto, A. C., Newton, E. R., et al.
 1175 2021, *AJ*, **161**, 171

- 1176 Ujjwal, K., Kartha, S. S., Mathew, B., Manoj, P., &
 1177 Narang, M. 2020, *AJ*, **159**, 166
- 1178 Van Eylen, V., Agentoft, C., Lundkvist, M. S., et al.
 1179 2018, *MNRAS*, **479**, 4786
- 1180 Van Eylen, V., Albrecht, S., Huang, X., et al. 2019, *AJ*,
 1181 **157**, 61
- 1182 Villa Vélez, J. A., Brown, A. G. A., & Kenworthy,
 1183 M. A. 2018, *RNAAS*, **2**, 58
- 1184 Vissapragada, S., Knutson, H. A., Jovanovic, N., et al.
 1185 2020, *AJ*, **159**, 278
- 1186 Vogt, S. S., Allen, S. L., Bigelow, B. C., et al. 1994,
 1187 SPIE Conference Series, ed. D. L. Crawford & E. R.
 1188 Craine, Vol. 2198
- 1189 Walkowicz, L. M., & Basri, G. S. 2013, *MNRAS*, **436**,
 1190 1883, arXiv: 1309.2159
- 1191 Wang, L., & Dai, F. 2019, *ApJL*, **873**, L1
- 1192 Wenger, M., Ochsenbein, F., Egret, D., et al. 2000,
 1193 *A&AS*, **143**, 9
- 1194 Wirth, C. P., Zhou, G., Quinn, S. N., et al. 2021, *ApJL*,
 1195 **917**, L34
- 1196 Wu, Y. 2019, *ApJ*, **874**, 91
- 1197 Yee, S. W., Petigura, E. A., & von Braun, K. 2017, *ApJ*,
 1198 **836**, 77
- 1199 Yelda, S., Lu, J. R., Ghez, A. M., et al. 2010, *ApJ*, **725**,
 1200 331
- 1201 Zari, E., Hashemi, H., Brown, A. G. A., Jardine, K., &
 1202 de Zeeuw, P. T. 2018, *A&A*, **620**, A172
- 1203 Zhou, G., Winn, J. N., Newton, E. R., et al. 2020, *ApJ*,
 1204 **892**, L21
- 1205 Zhou, G., Quinn, S. N., Irwin, J., et al. 2021, *AJ*, **161**, 2

1206

APPENDIX

1207 A. YOUNG, AGE-DATED, AND AGE-DATEABLE STAR COMPILED

1208 The v0.6 CDIPS target catalog (Table 3) includes stars that are young, age-dated, and age-dateable. By
 1209 “age-dateable”, we mean that the stellar age should be measurable at greater precision than that of a typical
 1210 FGK field star, through either isochronal, gyrochronal, or spectroscopic techniques. As in Bouma et al.
 1211 (2019), we collected stars that met these criteria from across the literature. Table 4 gives a list of the studies
 1212 included, and brief summary statistics. The age measurement methodologies adopted by each study differ: in
 1213 many, spatial and kinematic clustering has been performed on the Gaia data, and ensemble isochrone fitting
 1214 of the resulting clusters has been performed (typically focusing on the turn-off). In other studies however,
 1215 the claim of youth is based on the location of a single star in the color-absolute magnitude diagram, or on
 1216 spectroscopic information.

1217 One major change in Table 3 relative to the earlier iteration from Bouma et al. (2019) is that the extent
 1218 of Gaia-based analyses has now matured to the point that we can neglect pre-Gaia cluster memberships,
 1219 except for a few cases with spectroscopically confirmed samples of age-dated stars. The membership lists for
 1220 instance of Kharchenko et al. (2013) and Dias et al. (2014) (MWSC and DAML) are no longer required. This
 1221 is helpful for various post-processing projects, since the field star contamination rates were typically much
 1222 higher in these catalogs than in the newer Gaia-based catalogs.

1223 The most crucial parameters of a given star for our purposes are the Gaia DR2 source_id, the cluster
 1224 or group name (cluster), and the age. Given the hierarchical nature of many stellar associations, we do
 1225 not attempt to resolve the cluster names to a single unique string. The Orion complex for instance can be
 1226 divided into almost one hundred kinematic subgroups (Kounkel et al. 2018). (**Added: Based on Figure 1,**
 1227 **the δ Lyr cluster may also be part of a similar hierarchical association.**) Similar complexity applies to the
 1228 problem of determining homogeneous ages, which we do not attempt to resolve. Instead, we simply merged
 1229 the cluster names and ages reported by various authors into a comma-separated string.

1230 This means that the age column can be null, for cases in which the original authors did not report an age,
 1231 or for which a reference literature age was not readily available. Nonetheless, since we do prefer stars with
 1232 known ages, we made a few additional efforts to populate this column. When available, the age provenance
 1233 is from the original analysis of the cluster. In a few cases however we adopted other ages when string-
 1234 based cross-matching on the cluster name was straightforward. In particular, we used the ages determined
 1235 by Cantat-Gaudin et al. (2020) to assign ages to the clusters from Gaia Collaboration et al. (2018a), Cantat-
 1236 Gaudin et al. (2018), Castro-Ginard et al. (2020), and Cantat-Gaudin & Anders (2020).

1237 The catalogs we included for which ages were not immediately available were those of Cotten & Song
 1238 (2016), Oh et al. (2017), Zari et al. (2018), Gagné et al. (2018a), Gagné et al. (2018b), Gagné & Faherty
 1239 (2018), and Ujjwal et al. (2020). While in principle the moving group members discussed by Gagné et al.
 1240 (2018a,b); Gagné & Faherty (2018) and Ujjwal et al. (2020) have easily associated ages, our SIMBAD cross-
 1241 match did not retain the moving group identifiers given by those studies, which should therefore be recovered
 1242 using tools such as BANYAN Σ (Gagné et al. 2018b). We also included the SIMBAD object identifiers TT*,
 1243 Y*O, Y*?, TT?, and pMS*. Finally, we included every star in the NASA Exoplanet Archive planetary system
 1244 (ps) table that had a Gaia identifier available (Akeson et al. 2013). If the age had finite uncertainties, we also
 1245 included it, since stellar ages determined through the combination of isochrone-fitting and transit-derived
 1246 stellar densities typically have higher precision than from isochrones alone.

1247 For any of the catalogs for which Gaia DR2 identifiers were not available, we either followed the spa-
 1248 tial (plus proper-motion) cross-matching procedures described in Bouma et al. (2019), or else we pulled the
 1249 Gaia DR2 source identifiers associated with the catalog from SIMBAD. We consequently opted to drop the
 1250 ext_catalog_name and dist columns maintained in Bouma et al. (2019), as these were only popu-
 1251 lated for a small number of stars. The technical manipulations for the merging, cleaning, and joining were
 1252 performed using pandas (McKinney 2010). The eventual cross-match (using the Gaia DR2 source_id)
 1253 against the Gaia DR2 archive was performed asynchronously on the Gaia archive website.

1254

B. THE TRANSIT ASYMMETRY

1255

B.1. How Robust is the Asymmetric Transit?

1256 As a means of exploring the robustness of the transit asymmetry, Figures 9, 10, and 11 show the Kepler data
 1257 binned in three ways: over Kepler quarters, Julian years, and quartiles of local slope. Over Kepler quarters
 1258 (Figure 9), Quarter 6 shows the strongest asymmetry: a deviation of about 3 ppt from expectation. Quarter

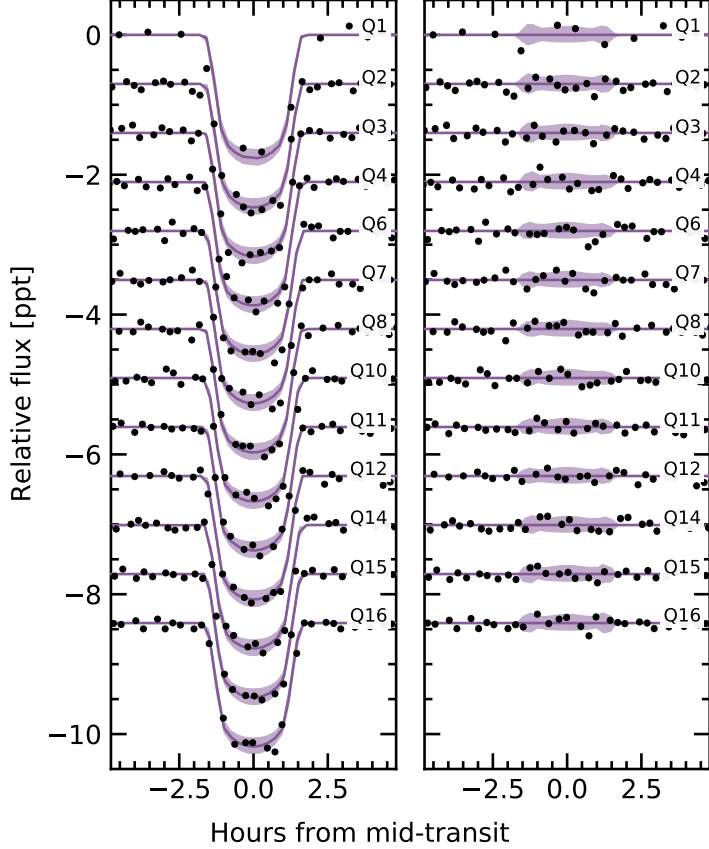


Figure 9. Transit model residuals through time (binned by Kepler quarter). *Left:* Phase-folded transit of Kepler 1627b, with stellar variability removed. Black points are binned to 20 minute intervals. The 2σ model uncertainties and the maximum *a posteriori* model are shown as the faint purple band, and the dark purple line. *Right:* As on the left, with the transit removed.

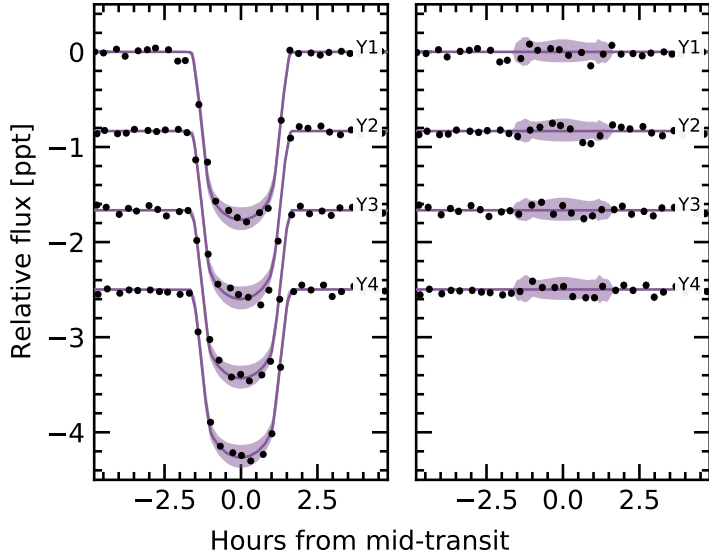


Figure 10. Transit model residuals through time (binned by year of observation). *Left:* Phase-folded transit of Kepler 1627b, with stellar variability removed. Points and models are as in Figure 9. *Right:* As on the left, with the transit removed.

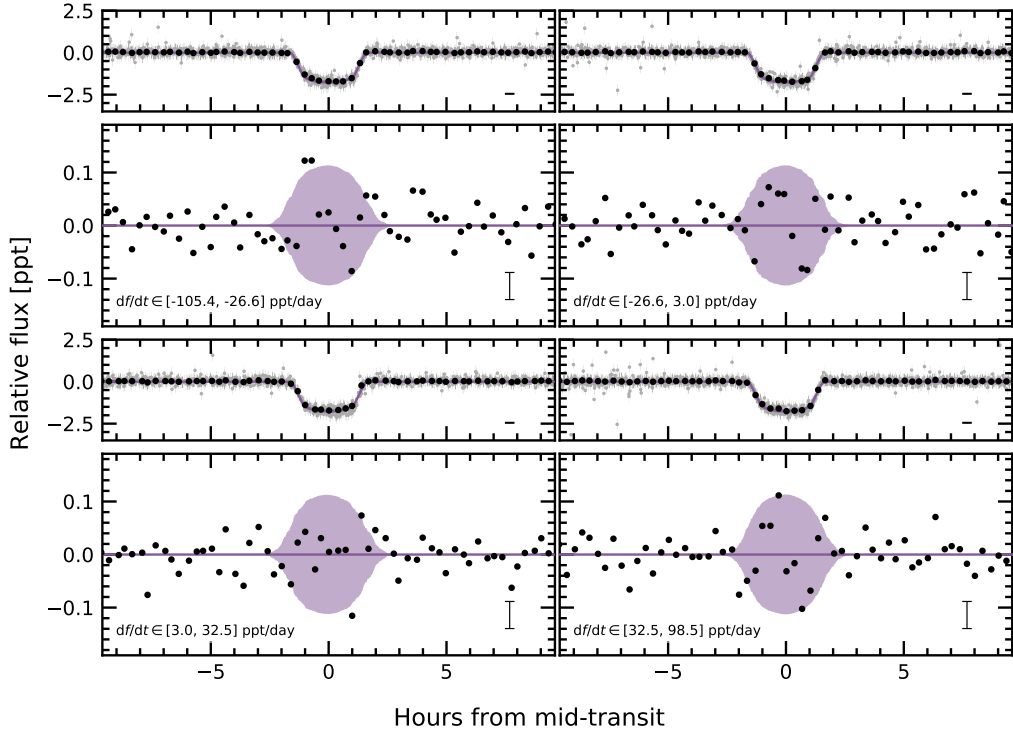


Figure 11. Transit models and residuals, binned by quartiles in the local slope of the light curve. Representative uncertainties for the black points (binned at 20 minute intervals) are shown in the lower right of each panel. A similar transit asymmetry to that shown in Figure 5 seems to be present in three of the four bins.

7 shows an anomaly at roughly the same transit phase. Year 2 correspondingly shows the strongest anomaly out of any year in Figure 10; the asymmetry is visually apparent however in each of the four years.

To bin by quartiles in local slope, we used our measurements of the local linear slopes in each of the observed transit windows (144 transits total). Four outlier transits were removed, leaving 140 transits. These were then divided into quartiles, so that each panel shows 35 transits binned together. The exact light curve slope intervals are listed in the lower left panels of Figure 11. Binned by local slope quartiles (Figure 11), the asymmetry is visually present in three of the four quartiles: the only bin in which it does not appear is $df/dt \in [3.0, 32.5] \text{ ppt day}^{-1}$.

Within the theory presented by Mazeh et al. (2015), unresolved starspot crossings cause the weak correlation between TTVs and the local light curve slope (Figure 6). In this model, we would expect the light curves with the most negative local slopes to have the largest positive TTVs, due to spot crossing events during the latter half of transit. The upper-left panel of Figure 11 agrees with this expectation. However, we would also expect the sign of the effect to reverse when considering the most positive local slopes (most negative TTVs). The lower-right panel of Figure 11 contradicts this expectation: the residual in both cases maintains the same parity! On the one hand, this shows that the residual is not dependent on the local light curve slope, which lowers the likelihood that it might be an artifact of our detrending methods. On the other, it raises the question of whether unresolved starspot crossings are indeed the root cause of the correlation shown in Figure 6. While we do not have a solution to this contradiction, the injection-recovery tests discussed in Section 4.1.3 provide some assurance that the TTV-slope correlation is not simply a systematic artifact.

B.2. Interpretation

The transit asymmetry seems robust against most methods of binning the data, though with some caveats (e.g., the “middle quartile” in local flux, $df/dt \in [3.0, 32.5] \text{ ppt day}^{-1}$, where the asymmetry does not appear). Nonetheless, if the asymmetric were systematic we might expect its parity to reverse as a function of the sign of the local slope, and it does not. We therefore entertained four possible astrophysical explanations: gravity darkening, transit timing variations, spot-crossing events, and a persistent asymmetric dusty outflow.

Gravity darkening is based on the premise that the rapidly rotating star is oblate, and brighter near the poles than the equator (e.g., Masuda 2015). The fractional transit shape change due to gravity darkening is on the order of $(P_{\text{break}}/P_{\text{rot}})^2$, for P_{break} the break-up rotation period, and P_{rot} the rotation period. Using

the parameters from Table 2, this yields an expected 0.14% distortion of the ≈ 1.8 ppt transit depth: *i.e.*, an absolute deviation of ≈ 2.5 ppm. The observed residual has a semi-amplitude of ≈ 50 ppm. Since the expected signal is smaller than the observed anomaly by over an order of magnitude, gravity darkening seems to be an unlikely explanation.

The scenario of transit timing variations (TTVs) producing the asymmetry seems unlikely because the transit timing variations we do observe are correlated with the local light curve slope, which increases roughly as much as it decreases. From our analysis, the mean TTV and its standard deviation are 0.66 ± 5.53 min; similarly the mean local slope and its standard deviation are 0.59 ± 45.50 ppt day $^{-1}$. There is therefore little expectation for TTVs to produce the asymmetry. A separate line of argument comes from Figure 11. If the local slope were essential to producing the transit asymmetry, we would expect that in the largest df/dt bin, $df/dt \in [3.0, 32.5]$ ppt day $^{-1}$, the sign of the asymmetry would reverse. We do not see evidence for this being the case.

The third and related possibility is that of starspot crossings. Young stars have higher spot-covering fractions than old stars (*e.g.*, Morris 2020). Young solar-type stars may also host dark starspots at high stellar latitudes (*e.g.*, EK Dra; Strassmeier 2009), though interferometric imaging of spotted giant stars has shown different starspot latitude distributions than those inferred from Doppler imaging (Roettenbacher et al. 2017). Regardless, for any spot-crossing anomalies to add coherently over the 140 Kepler transits, it seems likely that we would need either for spots to be persistent at a particular latitude (and for the planetary orbit to be somewhat misaligned), or for a “stroboscopic” longitudinal phasing (*e.g.*, Dai et al. 2018). For our system, $P_{\text{orb}}/P_{\text{rot}} \approx 2.76$, which means that every 4 transits and 11 stellar rotations, the planet crosses over roughly the same stellar longitude, which might enable the necessary phasing if the spot-groups are large and long-lived. Unfortunately, the S/N per Kepler transit is ≈ 8 , which renders individual spot-crossing events unresolved. This explanation seems marginally plausible, mainly because the expected spot-crossing anomaly amplitudes (≈ 100 ppm) resemble the observed amplitude of the asymmetry (≈ 50 ppm). One issue with this explanation however is that there is no reason to expect starspot crossing events to last exactly half the transit duration.

A persistent feature of the planet itself might therefore be needed to explain the transit asymmetry. An asymmetric outflow from the planet’s atmosphere could at least geometrically meet the requirements (*e.g.*, McCann et al. 2019). To explain the asymmetric transit, a small, dense component would lead the planet, and a long, more rarefied (and variable) component would trail it. This might also explain the slight flux decrement visible for ~ 1 hour pre-ingress (Figure 5). The amplitude of the asymmetry is roughly in line with theoretical expectations for dusty outflows (Wang & Dai 2019), and based on the planet’s size, its mass is likely in a regime where such outflows are possible. Out of the four explanations discussed, this one at least theoretically seems the most plausible. By composition, the expectation would be that the envelope is mostly hydrogen and helium gas, with a dust or haze component providing the broadband opacity in the Kepler bandpass. A natural path for testing this idea would be to observe additional transits of the planet in hydrogen absorption, metastable helium absorption, or across a broad wavelength range in the near-infrared.

C. SPECTROSCOPY AND PHOTOMETRY DURING THE TRANSIT OF 2021 AUG 7

We monitored Kepler 1627 with Keck/HIRES before, during, and after transit on the night of 2021 Aug 7. We used the iodine cell for wavelength calibration, and extracted the 1-D spectra using the standard California Planet Survey pipeline (Howard et al. 2010). The airmass ranged between 1.1 and 2.2 from the start through the end of observations; the seeing ranged from $1.^{\prime\prime}1$ at the beginning to $1.^{\prime\prime}5$ at the end. We also simultaneously observed across *griz* bands using MuSCAT3 at Haleakalā Observatory on Maui, HI. Performing aperture photometry on the latter image stack yielded the data given in Table 5.

We considered two approaches to measuring the velocities: in the first, hereafter “Method 1”, we cross-correlated against a template found via spectral classification with SpecMatch-Emp (Yee et al. 2017). In “Method 2”, we used a high S/N template of V1298 Tau. Although V1298 Tau is cooler than Kepler 1627A by ≈ 500 K, it has a comparable amount of line-broadening ($v \sin i = 23$ km s $^{-1}$), and a comparable level of stellar activity. The mean and standard deviation of the internal RV uncertainties averaged over all epochs were 16.2 ± 1.1 m s $^{-1}$ from Method 1, and 12.6 ± 0.6 m s $^{-1}$ from Method 2. The corresponding time-averaged reduced χ^2 from the template match was 1.57 ± 0.04 (Method 1) and 1.30 ± 0.02 (Method 2). Given these diagnostics, we adopted the velocities from the second approach, which are reported in Table 6.

Figure 7 shows the results. The MuSCAT3 photometry shows the expected starspot trend, along with the transit and what is likely a chromatic starspot crossing event at JD – 2459433 = 0.955. The radial velocities decrease by ≈ 250 m s $^{-1}$ over the six hour window. This decrease in RV is correlated with a decrease in the S-indices derived from the Ca HK lines. One outlying RV point is apparent shortly before egress; it is temporally coincident with an outlying value in the S-index time series.

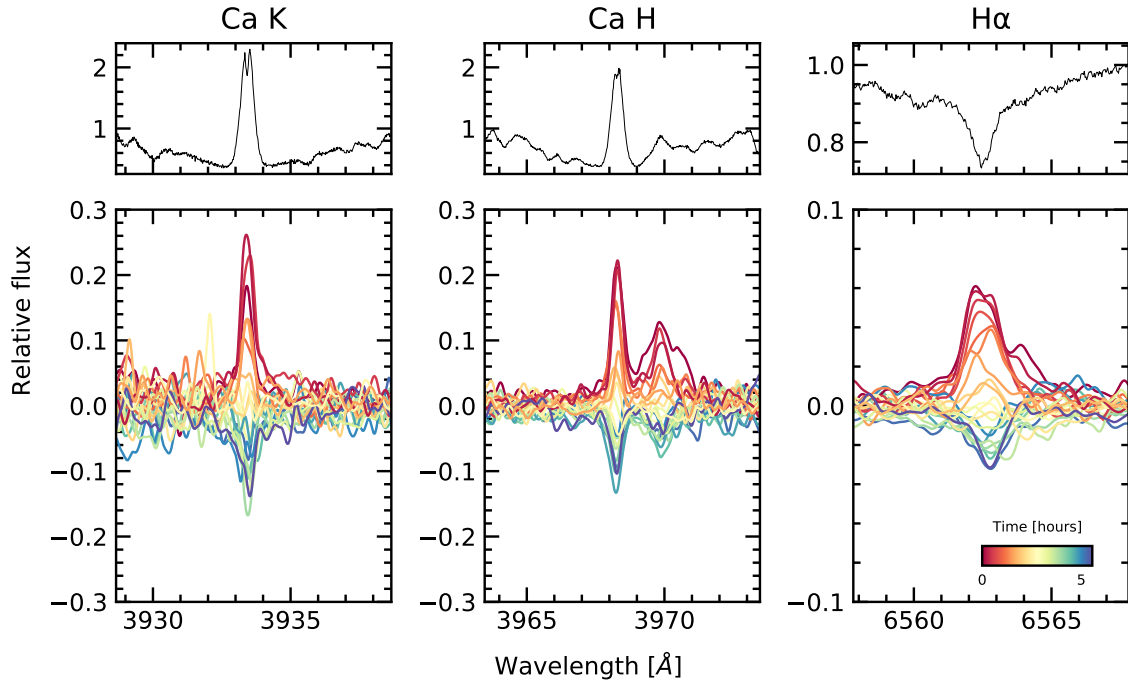


Figure 12. Spectroscopic activity indicators during the transit of 2021 Aug 7. The *top panels* show the median line profiles Ca K, Ca H, and H α line profiles from the HIRES spectra. The *lower panels* show the differences of each individual spectrum relative to the median spectrum. The bump in the red wing of Ca H is He. The spectra in the lower panels are smoothed for visualization purposes.

Overall, we expect the dominant trends in both the photometry and radial velocities to be caused by starspots on the stellar photosphere rotating into and out of view. The plasma in the leading and receding limbs of the stellar disk has an apparent line-of-sight velocity of $\pm 20 \text{ km s}^{-1}$. Over 10% of a rotation cycle ($P_{\text{rot}} = 2.6 \text{ days}$), spots near these limbs come into and out of view, modulate the stellar velocity profile, and can thereby produce the overall $\approx 250 \text{ m s}^{-1}$ trend. The Ca HK and H α emission profiles support this interpretation; Figure 12 shows that each line gradually decreases in intensity over the course of the six hour sequence.

The expectation however is for the starspot-induced signals to be smooth, at worst with contributions at $0.5 P_{\text{rot}}$ or $0.25 P_{\text{rot}}$ (Klein & Donati 2020). We therefore fitted the RVs using the Hirano et al. (2010, 2011) models for the Rossiter-McLaughlin (RM) effect, and allowed for an optional linear and quadratic trend in time to fit the $\approx 250 \text{ m s}^{-1}$ spot-induced trend. We followed the methodology developed by Stefansson et al. (2020). We allowed the sky-projected obliquity, the projected stellar equatorial velocity, and the Gaussian dispersion of the spectral lines to vary, and fixed the limb-darkening using the V-band tabulation from Claret & Bloemen (2011). We assumed a Gaussian prior on $v \sin i$ and a/R_{\star} from Table 1, and also allowed for a white-noise jitter term to be added in quadrature to the measurement uncertainties. We used a 15 minute exposure time to numerically evaluate the model.

The quadratic model with the RM effect is shown in Figure 7; the jitter term is incorporated in the model uncertainties, but not the plotted measurement uncertainties. The plotted measurement uncertainties are the internal uncertainties on the RVs ($\approx 13 \text{ m s}^{-1}$), and are dominated by the $v \sin i$ broadening. However, between exposures, the RVs show significant additional scatter that is not captured by the slow quadratic trend. The white-noise jitter for this particular model is $\sigma_{\text{RV}} = 27^{+6}_{-5} \text{ m s}^{-1}$, which is comparable to the expected RM anomaly of $\Delta v_{\text{RM}} \approx f_{\text{LD}} \cdot \delta \cdot v \sin i \cdot \sqrt{1 - b^2} \approx 20 \text{ m s}^{-1}$, assuming a perfectly aligned orbit.

The presence of this additional scatter prevents a convincing detection of the RM effect. The reason can be understood via model comparison. If we compare the model with a quadratic trend and the RM effect against a model with a linear trend and the RM effect, or even a model with no RM effect at all, then the respective

Bayesian Information Criterion (BIC) values are as follows.

$$\begin{aligned} \text{BIC} &= 227.1 \quad (\text{Quadratic+RM}) \\ \text{BIC} &= 231.1 \quad (\text{Linear+RM}) \\ \text{BIC} &= 221.4 \quad (\text{Only Quadratic}). \end{aligned} \quad (\text{C1})$$

1364 There is therefore no evidence to prefer the model with the RM effect against a model that only accounts
 1365 for the stellar variability. The “only quadratic” model does particularly well because it can inflate the jitter
 1366 term to account for scatter during the transit (even if the scatter contains astrophysics!), and it has fewer free
 1367 parameters. However, we cannot justify a physical prior on the jitter term, because we do not understand
 1368 the origin of the exposure-to-exposure scatter. As noted above, the velocity deviations from starspots are
 1369 expected to have contributions at the stellar rotation frequency, or harmonics thereof. This jitter is present on
 1370 the exposure timescale (15 minutes), which is only 0.4% of the stellar rotation period; it is not obvious that
 1371 starspots would be the culprit.

1372 The amplitude of both the spot-induced trend and the jitter are somewhat larger than recent comparable
 1373 measurements in systems such as AU Mic (Palle et al. 2020), DS Tuc (Montet et al. 2020; Zhou et al. 2020)
 1374 and TOI 942 (Wirth et al. 2021). One possible explanation for the jitter is that it is astrophysical in origin,
 1375 and that it is caused by some novel process operating on the surface of Kepler 1627A. Another possibility
 1376 is that our RV analysis underestimates our measurement uncertainties; in order to achieve the requisite time-
 1377 sampling the S/N per resolution element in our spectra was 70 to 80, which is lower than desired for deriving
 1378 high-precision velocities. In addition, the rapid rotation of the star could affect accuracy of the uncertainties
 1379 from the velocity extraction. Observations at higher S/N are necessary to distinguish these two possibilities,
 1380 and remain worthwhile in order to clarify the orbital geometry of Kepler 1627Ab. Useful next steps would
 1381 include transit observations with a stabilized spectrograph in the optical (e.g., Gibson et al. 2016; Seifahrt
 1382 et al. 2018), or in the near-infrared (e.g., Feinstein et al. 2021).

Table 5. MuSCAT3 photometry of Kepler 1627.

Time [BJD _{TDB}]	Rel. Flux	Rel. Flux Err.	Bandpass
2459433.829202	0.99719	0.00091	g
2459433.829324	0.99849	0.00112	r
2459433.829117	0.99611	0.00116	i
2459433.829406	0.99941	0.00136	z

NOTE— Table 5 is published in its entirety in a machine-readable format. Example entries are shown for guidance regarding form and content.

Table 6. Kepler 1627 radial velocities.

Time [BJD _{TDB}]	RV [m s^{-1}]	σ_{RV} [m s^{-1}]	S-value
2459433.801306	152.97	12.29	0.7355
2459433.812255	100.5	13.23	0.7434

NOTE— Table 6 is published in its entirety in a machine-readable format. Example entries are shown for guidance regarding form and content.

D. FLARE ANALYSIS

1383
 1384 In addition to the 3.9 years of long cadence data,
 1385 short cadence (1-minute) Kepler observations were
 1386 acquired over 97.7 days during Quarter 15. The
 1387 short cadence light curve shows a higher rate of
 1388 flaring than visible in the long cadence data (Figure
 1389 13). We analyzed the short cadence light curve
 1390 and its flares according to the following procedure.

- 1391 1. Fit the starspot-induced variability using a
 1392 Gaussian Process with a SHOTerm kernel,
 1393 a white-noise jitter term, and the mean flux.
- 1394 2. Select points more than twice the median ab-
 1395 solute deviation from the residual, and ex-
 1396 clude them from the light curve (these points
 1397 include the flares). Repeat Step 1.

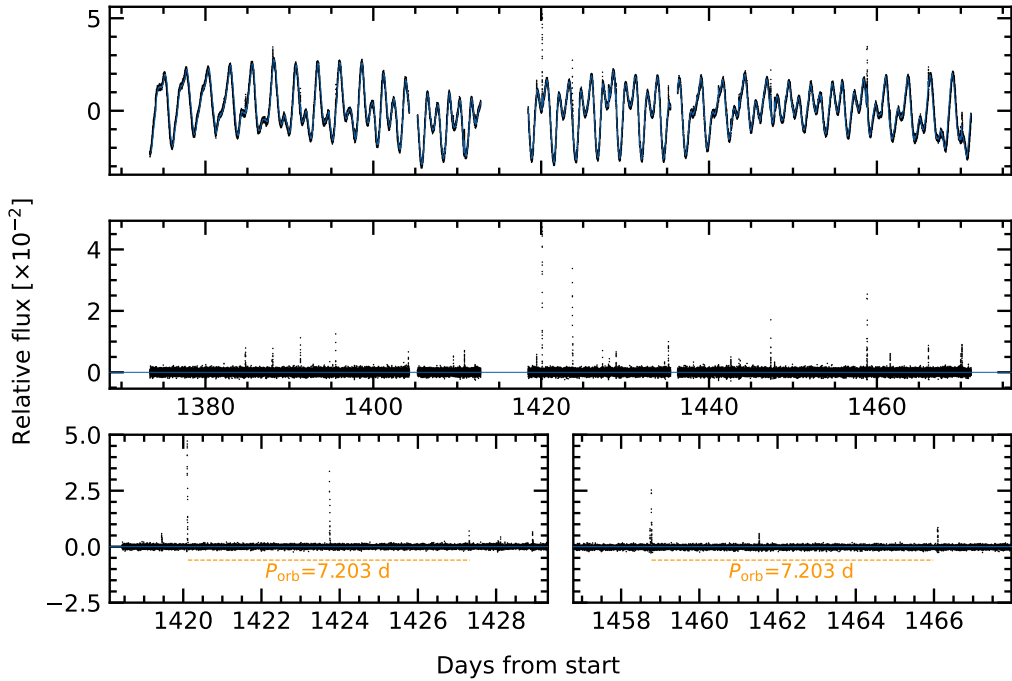


Figure 13. Flares in Kepler 1627. *Top:* The 1-minute cadence Kepler data (black points) is shown with a stellar variability model superposed (blue line). *Middle:* Residual after subtracting the stellar variability model. Flares appear as spikes. *Bottom:* Zooms of the brightest, and third-brightest flares. A timing coincidence – that both flares have “successors” approximately one (Added: planetary) orbital period after the initial event – is emphasized.

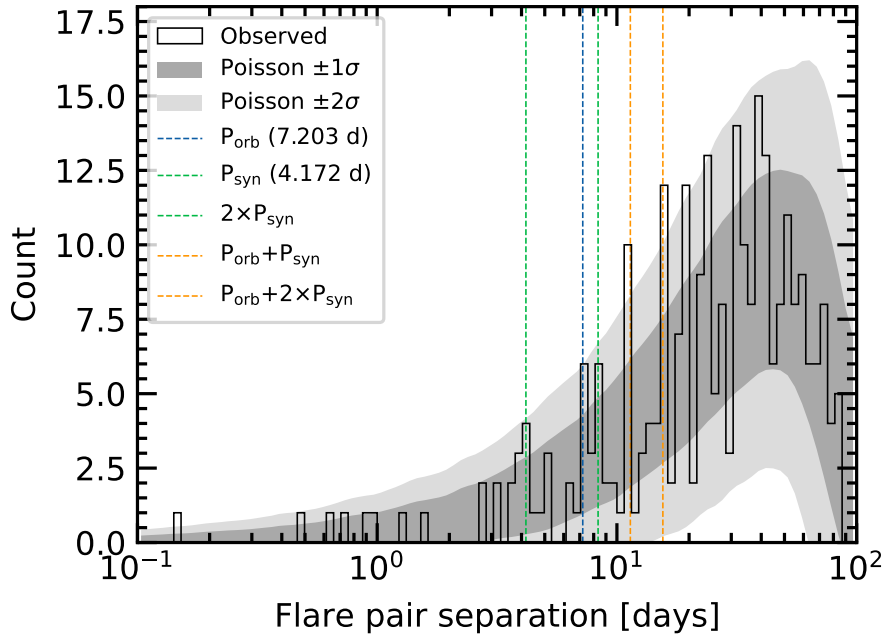


Figure 14. Statistics of inter-flare arrival times. 24 flares were recorded with amplitudes exceeding 0.5% over the 97.7 days of short cadence observations. The histogram of the time intervals between every possible pair of flares is shown in black. Some plausibly important timescales for star-planet interactions, namely the planetary orbital period and synodic period (the orbital period as seen from the rotating stellar frame) are shown along with their linear combinations. Monte Carlo draws from a Poisson distribution are shown with the gray bands. While peaks in the observed distribution do coincide with some of the “special periods”, the statistical evidence for a non-Poissonian process driving the flares does not clear the 5σ threshold.

1398 3. Using the residual from Step 2, identify all
 1399 flares, requiring them to be at least 20 ca-
 1400 dences apart, at least 7 median absolute de-
 1401 viations above the median baseline, and last-
 1402 ing at least 2 cadences in duration. Build the
 1403 mask spanning these times, from 5 minutes
 1404 before each flare begins to 2.5 minutes after
 1405 the final flare cadence. Repeat Step 1 a final
 1406 time.

1407 The final step of flare identification and fitting was
 1408 performed using `altaipony` (Davenport 2016;
 1409 Ilin et al. 2021). The analytic flare model is from
 1410 Davenport et al. (2014) and it parametrizes the flare
 1411 with a start time, an exponential lag time, and an
 1412 amplitude.

1413 There were $N_f = 24$ flares that exceeded 0.5% in
 1414 relative flux during the short cadence observations.
 1415 These 24 flares spanned a total of 6.5 hours (~ 15
 1416 minutes per flare). Inspecting the data, we noticed
 1417 a coincidence in the flare arrival times. The co-
 1418 incidence is that despite the low flare duty cycle,
 1419 one orbital period after the brightest flare, a second
 1420 flare followed. This and a similar event are shown
 1421 in Figure 13. The timing error is good to a $\approx 0.2\%$
 1422 difference from the orbital period, which given the
 1423 duty cycle seems *a priori* unlikely. If we consider
 1424 flares falling within 2% of the planet’s orbital pe-
 1425 riod after a previous flare, then 4 of the 24 flare
 1426 events have candidate “successors”.

1427 As with any coincidence, if one does not have a
 1428 firm prediction, it is difficult to assess whether a
 1429 surprise is statistically significant. Since our sur-
 1430prise was specifically at the inter-arrival time of
 1431 certain flares coinciding with special time inter-
 1432 vals, we performed the following analysis. First,
 1433 we considered all unordered pairs of flares. For
 1434 N flares there are $\binom{n}{2}$ such pairs (for our case,
 1435 276 pairs). We then compared the distribution of
 1436 the pair separations against that of a Poisson dis-
 1437 tribution. Specifically, we drew $N_f = 24$ samples
 1438 from a Poisson distribution with $\lambda = \Delta t / N_f$, for
 1439 $\Delta t = 97.7$ days the total duration of the observa-
 1440 tions, and repeated the draw 10^3 times with unique
 1441 random seeds.

1442 Figure 14 shows the results. The vertical lines
 1443 in the figure show the planetary orbital period,
 1444 the synodic period $P_{\text{syn}} = (P_{\text{rot}}^{-1} - P_{\text{orb}}^{-1})^{-1}$, and lin-
 1445 ear combinations thereof. The tidal period (half
 1446 the synodic period) is not shown. The bins are
 1447 logarithmically spaced to give 100 bins between
 1448 the minimum and maximum ordinate values. The
 1449 gray bands express the range of values observed
 1450 from the Poissonian draws. While it does seem
 1451 like an odd coincidence for peaks in the observed
 1452 flare arrival time distribution to coincide with the
 1453 locations of these “special intervals”, the statisti-
 1454 cal evidence for a non-Poissonian process driving

1455 the flares does not seem especially overwhelming.
 1456 More quantitatively, the peaks observed at the or-
 1457 bital and synodic periods are within the $\pm 2\sigma$ range
 1458 of a Poissonian process, and those at $P_{\text{orb}} + P_{\text{syn}}$ and
 1459 $P_{\text{orb}} + 2P_{\text{syn}}$ are only slightly above this range. With
 1460 that said, future analyses of these data by investiga-
 1461 tors with more knowledge of this topic could very
 1462 well yield more quantitative insights. Such analy-
 1463 ses should keep in mind an important caveat: the
 1464 amplitude distribution of M-dwarf flares extends
 1465 up to many times the quiescent flux (see Figure 7 of
 1466 Günther et al. 2020). A flare on Kepler 1627B pro-
 1467 ducing double its quiescent white-light flux would
 1468 yield a $\approx 1\%$ apparent amplitude. Such flares could
 1469 represent a significant fraction of those in the Ke-
 1470 pler observations.

List of Changes

Replaced: **mini-Neptune** replaced with: **planet**, on page 1.

Replaced: **main** replaced with: **prime**, on page 1.

Replaced: **through** replaced with: **with**, on page 1.

Replaced: **main** replaced with: **prime**, on page 2, line 74.

Replaced: **mini-Neptune** replaced with: **Neptune-sized planet**, on page 2, line 100.

Added: **to clarify the direction along which parallax uncertainties are expected to produce erroneous clusters**, on page 3.

Added: **we**, on page 2, line 136.

Added: **We calculated the tangential velocities for each of these stars relative to Kepler 1627 ($\Delta\mu^*$) by subtracting the observed proper motion from what the proper motion at the star's position would be if it were co-moving with Kepler 1627.**, on page 2, line 138.

Added: **in both physical and kinematic space**, on page 2, line 145.

Added: **One reason to suspect this is that the spread in tangential velocities exceeds typical limits for kinematic coherence (Meingast et al. 2021)**, on page 2, line 151.

Replaced: **the** replaced with: **this**, on page 2, line 158.

Deleted: **s** on page 2, line 159.

Added: **This also involved cuts on the photometric signal to noise ratio, the number of visibility periods used, the astrometric χ^2 of the single-source solution, and the $G_{\text{BP}} - G_{\text{RP}}$ color excess factor**, on page 3, line 183.

Replaced: **agree reasonably well with** replaced with: **are within a factor of two of**, on page 3, line 199.

Replaced: **from** replaced with: **in**, on page 3, line 201.

Added: **, and are all small enough that the choice of whether to use them vs. other extinction estimates does not affect our primary conclusions**, on page 5, line 204.

Deleted: **hybrid** on page 5, line 234.

Replaced: **to** replaced with: **and**, on page 5, line 235.

Replaced: **s 6 and 7** replaced with: **6**, on page 5, line 236.

Added: **To derive a probability distribution function for the age of δ Lyr cluster, we then assumed a Gaussian likelihood that treated the interpolated isochrones as the “model” and the δ Lyr cluster’s isochrone as the “data” (Equation 7 from Gagné et al. 2020).** The cluster’s age and its statistical uncertainty are then quoted as the mean and standard deviation of this age posterior., on page 5, line 238.

Added: **As a matter of scope, we restricted our attention to the 391 stars discussed in Section 2.1 in the spatial and kinematic proximity of Kepler 1627.**, on page 5, line 274.

Deleted: **As a matter of scope, we restricted our attention to the 391 stars discussed in Section 2.1 in the spatial and kinematic proximity of Kepler 1627.**, on page 5, line 293.

Replaced: **these** replaced with: **our 391**, on page 5, line 298.

Added: **from each other**, on page 6, line 316.

Replaced: **The other stars are likely to be field contaminants** replaced with: **Although some of these outlier stars might be unresolved F+K binaries that are in the cluster (Stauffer et al. 2016), assuming that they are field contaminants provides a more secure lower bound of the rotation period detection fraction.**, on page 6, line 322.

Replaced: **renormalized unit weight error (RUWE)**, replaced with: **RUWE**, on page 7, line 434.

Added: **(RUWE \approx 2.9; roughly the 98th percentile of the cluster’s distribution)**, on page 7, line 437.

Added: **Given that the secondary companion’s brightness in the Kepler band is \approx 1.5% that of the primary, source confusion for the rotation signal is not expected to be an issue.**, on page 7, line 475.

Replaced: **mini-Neptune** replaced with: **Neptune-**, on page 9, line 528.

Replaced: **main** replaced with: **prime**, on page 10, line 619.

Added: **This of course depends on the mass of Kepler 1627Ab; an alternative explanation for its large size could simply be that it is more massive than the typical Kepler mini-Neptune, or that it has an abnormally large envelope to core mass ratio.**, on page 12, line 786.

Added: **Based on Figure 1, the δ Lyr cluster may also be part of a similar hierarchical association.**, on page 21.

Added: **planetary**, on page 27.